

KEK Proceedings 2013-6  
October 2013  
R

# Proceedings of the Twentieth EGS Users' Meeting in Japan

August 8 - 9, 2013.  
KEK, Tsukuba, Japan

Edited by

Y. Namito, H. Hirayama and S. Ban



High Energy Accelerator Research Organization

**High Energy Accelerator Research Organization (KEK), 2013**

KEK Reports are available from:

High Energy Accelerator Research Organization (KEK)  
1-1 Oho, Tsukuba-shi  
Ibaraki-ken, 305-0801  
JAPAN

Phone: +81-29-864-5137  
Fax: +81-29-864-4604  
E-mail: [irdpub@mail.kek.jp](mailto:irdpub@mail.kek.jp)  
Internet: <http://www.kek.jp>

## FOREWARD

The Twentieth EGS Users' Meeting in Japan was held at High Energy Accelerator Research Organization (KEK) from August 8 to 9. The meeting has been hosted by the Radiation Science Center. More than 100 participants attended the meeting.

The meeting was divided into two parts. Short course on EGS was held at the first half of the workshop using EGS5 code. In the later half, 10 talks related EGS were presented. The talk covered the wide fields, like the medical application and the calculation of various detector responses *etc.* These talks were very useful to exchange the information between the researchers in the different fields.

Finally, we would like to express our great appreciation to all authors who have prepared manuscript quickly for the publication of this proceedings.

Yoshihito Namito  
Hideo Hirayama  
Syuichi Ban  
Radiation Science Center  
KEK, High Energy Accelerator Research Organization

## CONTENTS

<b>X-ray Computed Tomography Reconstruction using Scattered Radiation 1</b> <i>K. Takemoto, Y. Yamazaki, and N. Toda</i>	
<b>Verification of In-Phantom X-ray Energy Spectra in Dual-Energy Computed Tomography</b> <i>T. Ishii, H. Numamoto, Y. Hirai, S. Koyama, M. Kawano, and K. Ohashi</i>	9
<b>Quasi-Monoenergetic Photon Field of 200 keV using a Radioactive Source with Back-scatter Layout</b> <i>S. M. Tajudin, Y. Namito, T. Sanami, H. Hiaraya, and H. Iwase</i>	15
<b>Calculation of Dose Rate Distributions for a Ruthenium Ophthalmic Applicator</b> <i>M. Kato, T. Kurosawa, and N. Saito</i>	24
<b>Effect of the Difference in Electron Cutoff Energy on Surface Dose Calculation in the Monte Carlo Linear Accelerator Simulation of Megavoltage Photon Beams</b> <i>A. Takeuchi, T. Raich, R. Yoshida, K. Kojima, M. Niwa, M. Komori, and H. Oguchi</i>	30
<b>Evaluation of S Values of <math>^{99m}\text{Tc}</math> for Multi-Region Models of Kidneys in the ICRP Voxel Phantoms</b> <i>S. Hato and S. Kinase</i>	37
<b>Investigation of Backscatter Factor in Mammography using EGS5</b> <i>H. Numamoto, T. Ishii, Y. Hirai, and S. Koyama</i>	45

# X-ray Computed Tomography Reconstruction using Scattered Radiation

Kazuma Takemoto, Yoichi Yamazaki, Naohiro Toda

*Information and Computer Sciences, Aichi Prefectural University*

## abstract

In conventional X-ray CT (computed tomography), which uses a fan-shaped X-ray beam (fan-beam), the content ratio of scattered radiation is low; the influence of scattered radiation is assumed to be small. In recent years, cone-beam geometry has been adopted, whereby the content ratio of scattered radiation increases with an increase in cone angle. However, conventional image reconstruction methods do not adequately address scattered radiation because of problems such as computational complexity. Therefore, in cone-beam CT, when the conventional image reconstruction method is used, the influence of scattered radiation appears as an artifact in a reconstructed image. In this study, Monte Carlo simulation implemented in EGS5 is employed for image reconstruction. Presuming the existence of scattered radiation, we propose an image reconstruction algorithm based on successive optimization to minimize I-Divergence, which is equivalent to the likelihood function. Finally, we show the validity of the proposed method.

## 1 Introduction

X-ray CT (computed tomography) is a medical diagnostic imaging technique that is used to reconstruct cross-sectional images of an object from X-ray intensities measured using a rotating X-ray source-detector pair. X-ray CT was developed in the 1970s and is still indispensable to medical diagnostics, even though new diagnostic imaging techniques such as SPECT (single photon emission computed tomography), PET (positron emission tomography), and MRI (magnetic resonance imaging) have been developed.

In cone-beam geometry, which has been adopted in recent years, the content ratio of scattered radiation increases with an increase in cone angle [1]. In this method, the conventional image reconstruction method based on Lambert-Beer's law, in which scattered radiation is not included, may cause artifacts. To prevent the occurrence of artifacts, the anti-scatter grids (or collimators) are positioned in front of the detectors.

However, because scattered radiations cannot be obtained without objects, they should be recognized as carriers of the object's information and not as obstructives. Therefore, if a method that extracts object information from scattered radiations is available, we can obtain images of a higher quality using scattered radiation, under a general property of photon arrival that more photons improve image quality. This means that removing grids can potentially decrease the patient's exposure.

In recent years, high-speed computers have gained popularity with advancements in related technologies, and it has become possible to estimate the influence of scattered radiation via Monte

Carlo simulation [2].

In this paper, we extend our previous study [3] by proposing an image reconstruction algorithm based on successive optimization, which includes a projection simulation using EGS5 (a simulator that performs transport calculation by the Monte Carlo method), and we show the validity of the proposed method compared to the conventional reconstruction method, which assumes that CT devices are equipped with the anti-scatter grid. In this paper, we simplify the conditions using a monochromatic X-ray.

## 2 Reconstruction Method under the Presence of Scattered Radiation

If the conventional image reconstruction method is applied to the measured data containing scattered radiation, the influence of scattered radiation appears as artifacts in the reconstructed image. To overcome this problem, it is necessary to use a reconstruction method that reflects the influence of scattered radiation. Herein, we propose a new iterative technique utilizing the simulation of scattered radiation to improve the accuracy of the reconstructed image. In this section, we describe an iterative algorithm that employs I-Divergence as an evaluation function. Furthermore, a new image reconstruction method using EGS5 is proposed.

### 2.1 Iterative Reconstruction Method using I-Divergence as an Evaluation Function

Iterative reconstruction using the least-squares method has been adopted since the initial stages of CT development. Several recent studies have used the likelihood function to improve the performance of iterative reconstruction. In this study, we use I-Divergence, which is equivalent to the likelihood function, introduced by O’Sullivan et al.[4]. I-Divergence,

$$I = \sum_{\tau \in \mathbf{T}} Im(\tau) \log \frac{Im(\tau)}{\widehat{Im}(\tau)} - Ims(\tau) + \widehat{Im}(\tau), \quad (1)$$

is employed as a cost function to be minimized, where  $\mathbf{T}$  denotes a set of scanning positions  $\tau$ . I-Divergence comprises the actual measured value  $Im(\tau)$  and calculated value of the model,  $\widehat{Im}(\tau)$ .

In the conventional method, iterative reconstruction is performed on an initial image  $x_0$  until the behavior of the evaluation function (1) is sufficiently relaxed. The number of iterations is set to 10000.

### 2.2 Proposed Method

In this section, we propose a new method for image reconstruction. The image reconstruction algorithm using Monte Carlo simulation is shown below.

1. Set an initial image  $x_0$ .

2. After  $k$  iterations, a density map (a distribution of attenuation coefficient of water) is created. Calculate the amount of scattered radiation  $\hat{\beta}(\tau)$  via Monte Carlo simulation using EGS5 and the abovementioned density map.
3. Renew  $\hat{I}_m(\tau)$  by  $\hat{I}_m(\tau) = I_m(\tau) - \hat{\beta}(\tau)$ .
4. Repeat 2 and 3 until the behavior of the evaluation function (1) is sufficiently relaxed.

In this algorithm, scattered radiation is estimated at every  $k$ -time update of the image. The number of times scattered radiation is estimated is denoted by  $M$ . Therefore, the upper limit of the total number of iterations is  $k * M$ . The flow chart is shown in Figure 1 (where  $i$  denotes the number of iterations and  $j$  denotes the number of times scattered radiation is estimated).

In this study, we set  $k$  to 1000,  $M$  to 10, and  $k * M$  to 10000.

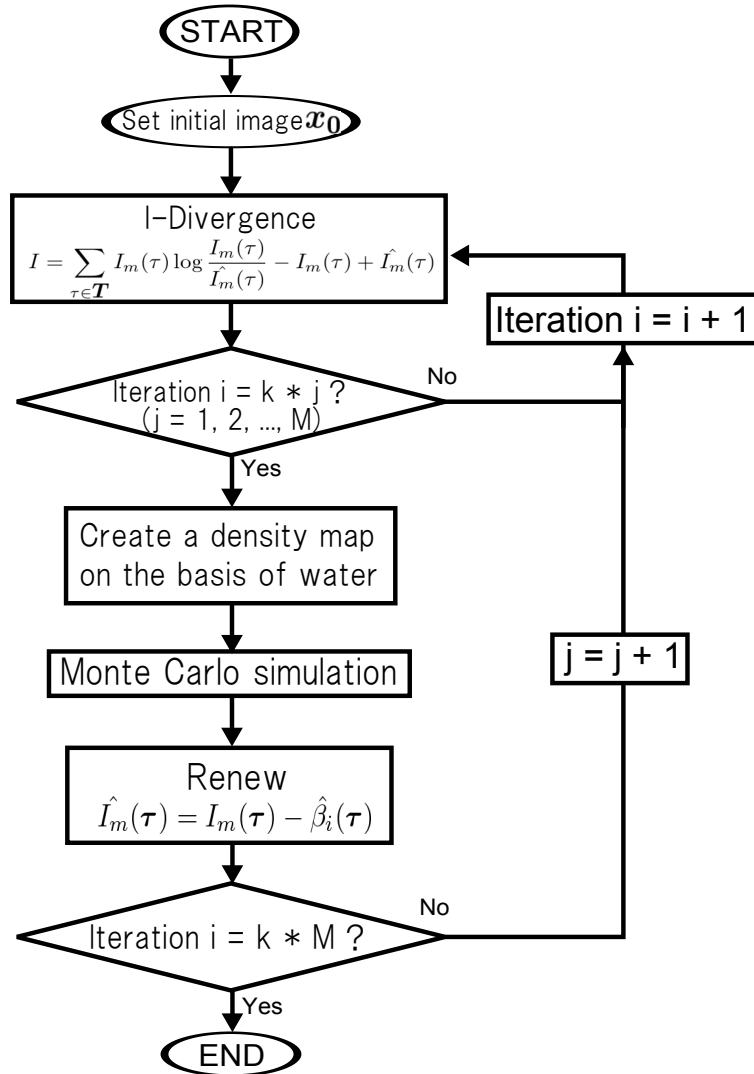


Figure 1: Flow chart of the proposed method

### 3 Numerical Experiments

In this section, we show the validity of the proposed method via numerical experiments.

#### 3.1 Geometry of Simulation

The number of photons at a single energy of 100 [keV] is set to  $10^5$ , the number of divisions in the rotation angle is set to 128, and the number of NaI detectors is set to 64. The objective space is a rectangle of size 30 [cm]  $\times$  30 [cm]  $\times$  18.75 [cm]. The phantom shown in Figure 2(a) is a water-filled sphere having a diameter of 22 [cm]. Two spheres having a diameter of 4 [cm] and composed of a cortical bone are arranged symmetrically in the water-filled sphere. This is considered as the ideal phantom.

In the experiments, the ideal phantom is used after adequately discretizing the space. We use a phantom that has  $8 \times 8$  voxels, as shown in Figure 2(b). The distance between the X-ray focus and the iso-center is 30 [cm], which is equal to the distance between the detectors and the iso-center. The X-ray tube radiates a cone-beam whose fan angle  $\theta$  and cone angle  $\Phi$  are 90 [deg] and 5 [deg], respectively, as shown in Figure 3. The geometry is modeled as shown in Figure 4.

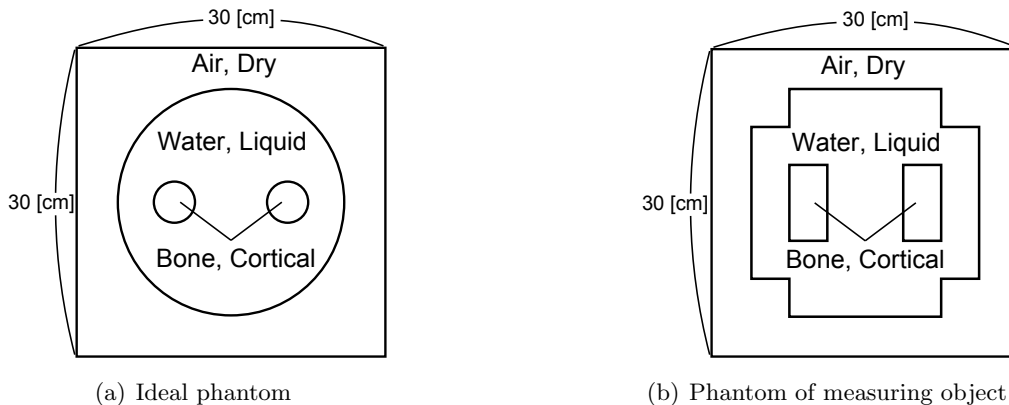


Figure 2: Phantom

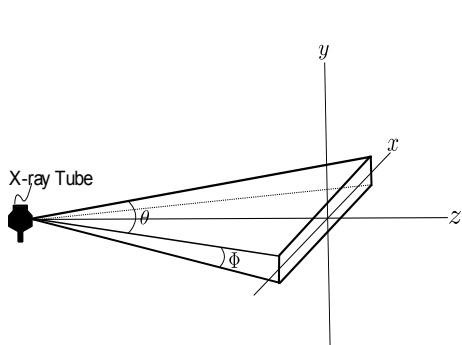


Figure 3: Shape of X-ray beam

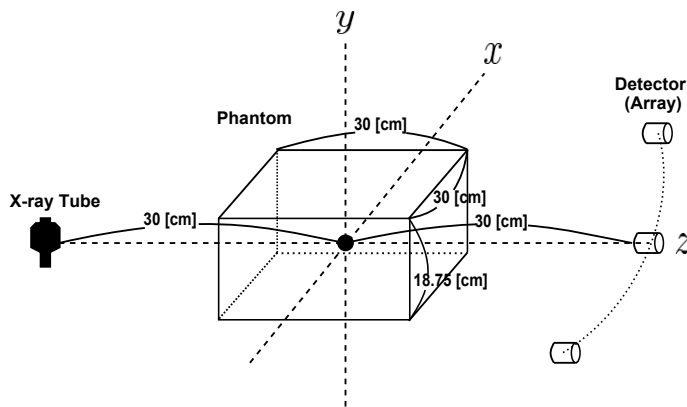


Figure 4: Geometry

### 3.2 Verification of Reconstructed Images

In this section, the quality of the reconstructed images obtained using the proposed method and the conventional method is compared. A true image, which indicates the true attenuation coefficient, is shown in Figure 5. We adopt an image (shown in Figure 6) that is reconstructed by the filtered back-projection method using measured intensity, and it contains scattered radiation as the initial image.

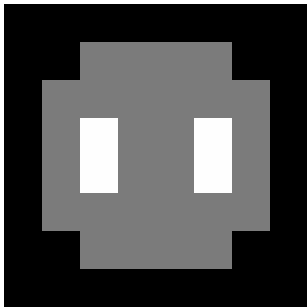


Figure 5: True reconstruction picture

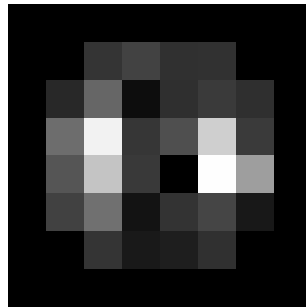


Figure 6: Initial picture

If the proposed method is effective, the reconstructed image obtained using the proposed method, which uses the data that contains scattered radiation, should have a smaller error than that of the conventional method, which uses data that does not contain scattered radiations. The reconstructed image for different numbers of iterations obtained using both the conventional method and the proposed method are shown in Figure 7. In Figure 7, the figures (a)-(f) indicate the following: (a) shows the image obtained using the conventional method for the measured value without scattered radiation, (b) shows the image obtained using the conventional method for the measured value with scattered radiation, and (c)-(f) show the images obtained using the proposed method for the measured value with scattered radiation for different numbers of iterations.

From Figure 7, it is observed that as the number of iterations increases, the accuracy of the reconstructed image obtained using the proposed method also increases.

### 3.3 Evaluation of Attenuation Coefficient

The error of the reconstructed image is given by the root-mean-square error of the attenuation coefficient as follows:

$$Error = \frac{1}{N} \sqrt{\sum_{i=1}^N \frac{(\mu_i - \hat{\mu}_i)^2}{\mu_i}} \quad , \quad (2)$$

where  $N$  denotes the number of space division,  $\mu_i$  denotes the true attenuation coefficient at 100 [keV], and  $\hat{\mu}_i$  denotes the attenuation coefficient obtained by each reconstruction method. Figure 8 shows the error of the attenuation coefficient plotted against the number of iterations.

From Figure 8, it is clearly observed that as the number of iterations increases, the error decreases. In addition, the error obtained with the proposed method is lower than that with the conventional method.

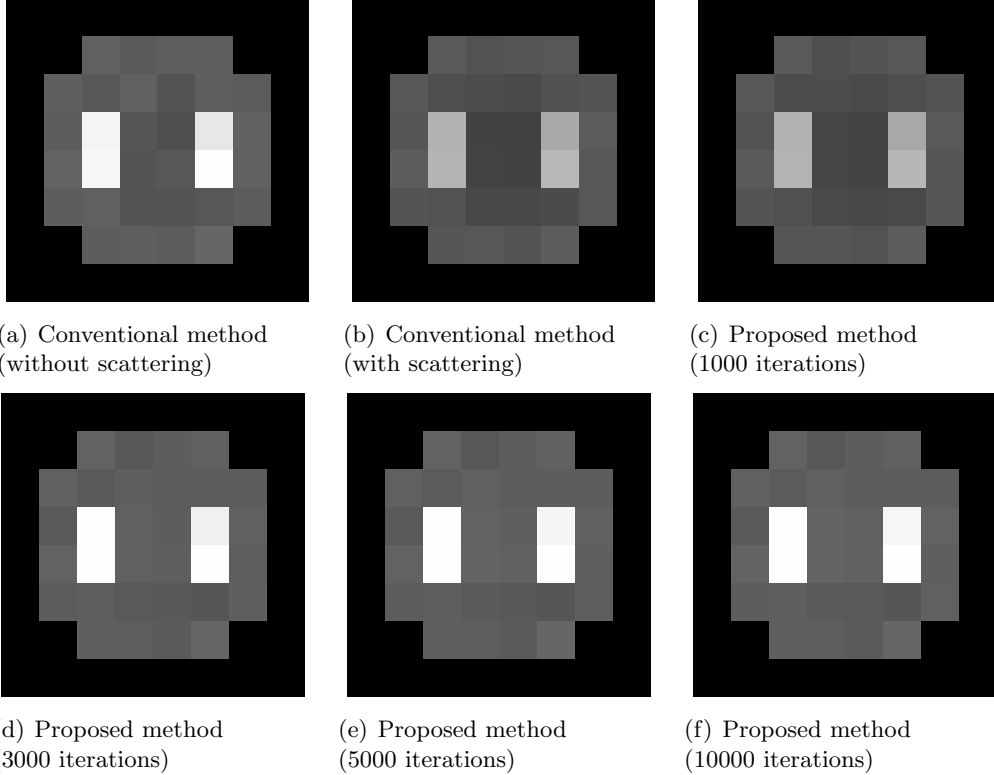


Figure 7: Reconstructed images

### 3.4 Accuracy of Scattered Radiation Estimation

If the scattered radiation is not estimated with sufficient accuracy, an improvement in the reconstructed image cannot be observed, as mentioned previously. In this section, we observe how the scattered radiation is accurately estimated in the proposed method. Figure 9(a) and (b) show the estimated amount of scattered radiation after 2000 and 10000 iterations, respectively.

The root-mean-square error of the scattered radiation,

$$Error = \frac{1}{N} \sqrt{\sum_{i=1}^N \frac{(\beta_i - \hat{\beta}_i)^2}{\beta_i}}, \quad (3)$$

is employed as an evaluation criterion, where  $N$  denotes the number of space divisions,  $\beta_i$  denotes the true scattered radiation, and  $\hat{\beta}_i$  denotes the estimated scattered radiation in each iteration.

From Figure 10, it is observed that as the number of iterations increases, the shapes of the estimated scattered radiation approach the true shapes. Thus, we have shown the validity of the proposed method.

## 4 Conclusion

In this study, we proposed an image reconstruction algorithm by considering scattered radiation, and we demonstrated an example to show that positive utilization of the scattered radiation results in a small reconstruction error. For future research, it is necessary to verify that the proposed

method can reduce exposure and to increase the number of divisions in the objective space to apply the proposed method for practical use.

## References

- [1] K. Tokumoto, Y. Yamazaki, N. Toda, S. Shuji, The Radiological Society of North America (RSNA) 98th Scientific Assembly and Annual Meeting, SSG16-02, Chicago, IL, USA, Nov 2012.
- [2] H. Hirayama, Y. Namito, A. F. Bielajew, S. J. Wilderman, W. R. Nelson, "The EGS5 Code System, 2005-8, SLAC-R-730", Radiation Science Center Advanced Research Laboratory, High Energy Accelerator Research Organization (KEK), Stanford Linear Accelerator Center, Stanford, CA, 2005.
- [3] K. Takemoto, K. Tokumoto, Y. Yamazaki, N. Toda, "X-ray Computed Tomography in Consideration of the Influence of Scattered Radiation", KEK Proceedings, 2012.
- [4] J. A. O'Sullivan, J. Benac, IEEE Trans. Med. Imaging, Vol. 26, No. 3, pp. 283-297, 2007.
- [5] Y. Yamazaki, N. Toda, "Cone-Beam Dual-Energy CT Using an Asymmetric Filter", The Institute Of Electronics, Information and Communication Engineers D, Vol. J94-D, No. 7, pp. 1154-1164, 2011.

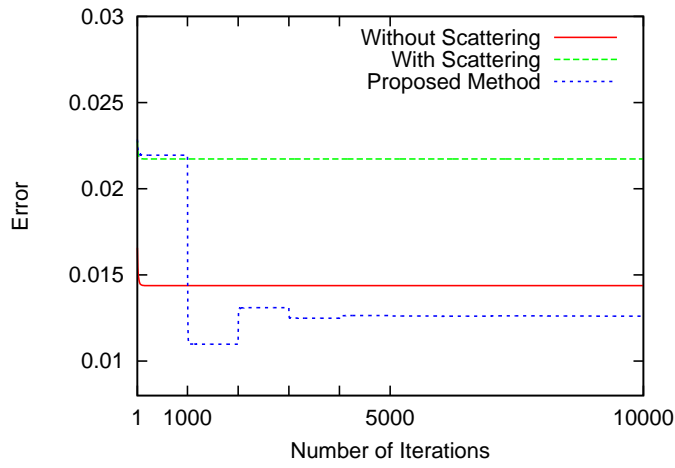


Figure 8: Root-mean-square errors of the attenuation coefficient

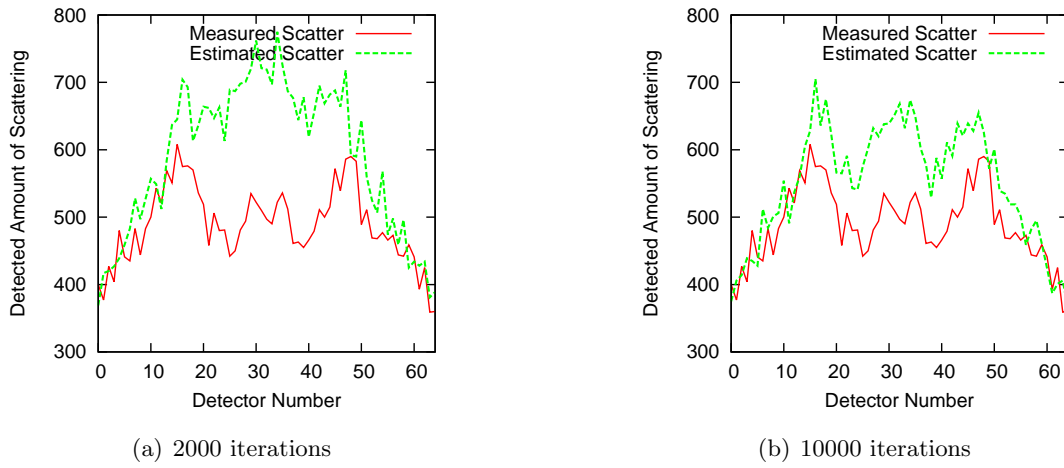


Figure 9: Scattered radiation

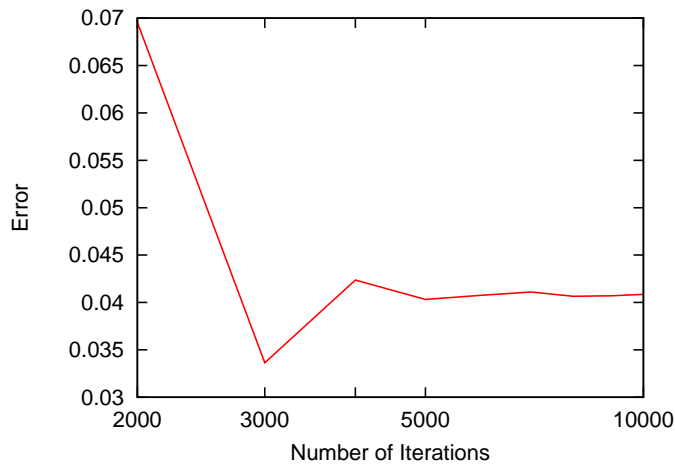


Figure 10: Root-mean-square errors of the scattered radiation

# VERIFICATION OF IN-PHANTOM X-RAY ENERGY SPECTRA IN DUAL-ENERGY COMPUTED TOMOGRAPHY

T. Ishii<sup>1</sup>, H. Numamoto<sup>1</sup>, Y. Hirai<sup>2</sup>, S. Koyama<sup>2</sup>, M. Kawano<sup>3</sup>, and K. Ohashi<sup>3</sup>

<sup>1</sup>*Department of Radiological Technology, Graduate School of Medicine, Nagoya University*

*1-1-20 Daiko-Minami, Higashi-ku, Nagoya 461-8673, Japan*

<sup>2</sup>*Central Department of Radiology, Nagoya City University Hospital,*

*1-Kawasumi, Mizuho-cho, Mizuho-ku, Nagoya 467-8602, Japan*

<sup>3</sup>*Department of Radiological Technology, School of Health Science, Nagoya University*

*1-1-20 Daiko-Minami, Higashi-ku, Nagoya 461-8673, Japan*

*e-mail: ishii.takanori@a.mbox.nagoya-u.ac.jp*

## Abstract

An in-phantom dosimetry system using pin silicon photodiodes was developed and used for measuring the radiation dose during X-ray computed tomography. The dosimeter sensitivity depends on the X-ray energy and is corrected using conversion factors for the effective energy of the incident X-rays. The main purpose of this study is to evaluate the system errors due to changes in the effective energies of in-phantom X-rays using an Electron Gamma Shower ver.5 (EGS5) Monte Carlo simulation. Continuous energy spectra of the incident X-rays on each photodiode dosimeter during dual-energy computed tomography scanning were obtained using the Monte Carlo simulation. The system errors were assessed by comparing the conversion factors for the incident and in-phantom X-rays. The result of this study indicates that specific organ doses could be overestimated. The maximum error in the organ doses was about 12%.

## 1. Introduction

In recent years, dual-energy computed tomography (DECT) imaging has become a valuable diagnostic technique. DECT uses two different kilovoltage energies nearly simultaneously during the same imaging session. Scanning with different tube voltages improves the characterization of various materials because of the inherent changes in the CT absorption parameters at different kilovoltage energies. DECT imaging has the potential to improve the detection of malignant liver tumors, enable the determination of urinary stone composition in vivo, and expedite the postprocessing of cardiac and abdominal CT angiography. DECT typically uses a higher energy (e.g., 140 kVp) than the energy (e.g., 100 or 120 kVp) used in routine single-energy CT (SECT), and the dose increases as the tube voltage increases. Hence, evaluations of the radiation dose to patients undergoing DECT scans have been regarded as essential. A method of evaluating the radiation dose for DECT, however, has never been established. Currently, the CT dose index (CTDI) for DECT is measured and used as reference radiation dose.

An in-phantom dosimetry system using pin silicon photodiodes was developed and used for measuring the radiation dose during X-ray CT and diagnostic radiography [1]. This in-phantom dosimetry system consists of an anthropomorphic phantom and photodiode dosimeters. These dosimeters were installed at the positions of various tissues and organs to evaluate the absorbed doses and effective dose. Although the photodiodes were applied as a small, highly sensitive X-ray sensor used in a diagnostic energy region, their sensitivity depends on the X-ray energy. This energy

dependence of the sensitivity is corrected using conversion factors for the effective energy of the incident X-rays, where the conversion factors are the inverse of the dosimeter sensitivity obtained using a sensitivity calibration curve obtained before making measurements. This is based on the understanding that the incident and in-phantom effective energies differ little at a tube voltage of 120 kVp and an effective energy of about 50 keV. The energy spectra or effective energies of X-rays observed in a phantom, however, could differ from those of the incident X-rays when a relatively high tube voltage (e.g., 140 kVp) is used.

In this study, the energy spectra or effective energies of in-phantom X-rays were investigated using an Electron Gamma Shower ver.5 (EGS5) Monte Carlo simulation. The system errors due to changes in the effective energies were evaluated.

## **2. Materials and Methods**

### **2.1 In-phantom dosimetry system using pin silicon photodiodes**

An in-phantom dosimetry system was constructed using an anthropomorphic phantom (THRA1, Kyoto Kagaku, Kyoto, Japan) composed of lung, bone, and soft tissue. The phantom represented a standard Japanese adult male; its height was 170 cm, and its mass was 60 kg. The pin silicon photodiodes used as X-ray dosimeters were implanted in the phantom. The photodiodes had a relatively large sensitive area of  $2.8 \times 2.8 \text{ mm}^2$ . The number of dosimeters was 48, and they were installed at the positions of various organs and tissues assigned according to the definition of the effective dose by the International Commission on Radiological Protection, Publication 103. [2] Figure 1 shows a schematic of the anthropomorphic phantom and the correspondences between the organs and the photodiode sensors. The in-phantom dosimetry system contained a data analysis program. The output voltage signals generated by the photodiode dosimeters were read out with a personal computer through an analog-to-digital converter. The signals were converted into the absorbed doses for each organ and tissue at the effective energy of the X-rays used.

### **2.2 Measurement using DECT scanner**

X-ray CT equipment is generally equipped with a beam-shaping filter in front of the X-ray tube radiation window. The X-ray energies and doses at each angle in the X-ray fan beam are adjusted by this beam-shaping filter. To simulate a DECT scan, X-ray fan beam data consisting of the actual dose profiles and X-ray energies were measured with a DECT scanner (SOMATOM Definition Flash, Siemens AG, Erlangen, Germany). The DECT scanner has two X-ray tubes, A and B, which were offset at an angle of  $95^\circ$ . X-rays with different kilovoltage energies were output from each of the X-ray tubes. The X-ray fan beam data and dose profiles were measured free in air by setting the cylindrical ion chamber on a base of polystyrene foam to obtain the data at each angle in the X-ray fan beam.

Measuring the continuous X-ray energy spectrum at each angle in the X-ray fan beam with a radiation spectrometer requires considerable effort and time. Hence, the half-value layer (HVL) of aluminum at each tube voltage was measured instead of the energy spectrum. The tube voltages of X-ray tube A were 100 and 120 kVp and those of X-ray tube B with a stannum filter were 140 kVp; these values correspond to the tube voltages used in SECT and DECT scans. The X-ray energy spectra were calculated from the measured HVLs.

The CTDI was measured for two CT scans using a polymethyl methacrylate (PMMA) cylindrical phantom 320 mm in diameter and a CT ion chamber 100 mm in length. The CT scans were carried out with single energy of 120 kVp and dual energies of 100 and 140 kVp. The CTDI was measured by setting the PMMA phantom on a thin plate of wood having a relatively low X-ray dose absorption to remove the effect of X-ray scattering and attenuation by the CT bed. The dose measurements were made in the center and in four peripheral locations (above, below, right, and left) around the phantom. Each SECT and DECT scan was repeated three times, and the CTDI was taken as the mean value of the doses.

### **2.3 CT simulation geometry**

In this simulation, a voxelized mathematical phantom (voxel phantom) was developed on the basis of the X-ray CT images of the anthropomorphic phantom used for the in-phantom dosimetry system. The DICOM images of the

phantom were converted to voxel data. The voxel size was  $3.2 \times 3.2 \times 10.0 \text{ mm}^3$ . The photodiode dosimeter regions were incorporated into the voxel phantom. To match the geometry of the SOMATOM Definition Flash DECT unit, the changes in the energy spectra and dose profiles of the X-ray fan beam due to the beam-shaping filter were incorporated into the simulation. Several energy spectra modeled by Tucker et al. were incorporated into this simulation; they were calculated for the maximum energy (tube voltage) and the measured HVL of aluminum. [3] The X-ray fan beam angles were  $42^\circ$  for X-ray tube A and  $32^\circ$  for X-ray tube B, and the beam width at the center of rotation was 32 mm. The source-to-isocenter distance was 600 mm, and the source was rotated  $360^\circ$  in  $1^\circ$  steps around the voxel phantom. DECT and SECT scans were simulated.

## 2.4 Energy spectra of incident X-rays on photodiode dosimeters

The X-ray energy spectra at each photodiode dosimeter location were obtained using the above simulation. The HVLs of aluminum were calculated from each incident X-ray energy spectrum, and each HVL was converted to an effective energy. The sensitivity calibration curve showing the dependence on the X-ray energy used in the in-phantom dosimetry system is shown in Figure 2 [1], where the sensitivities were functions of the effective energy. This sensitivity calibration curve could be used to derive the conversion factors for converting the output voltage from the photodiode dosimeters to the absorbed dose for soft tissue at the effective energy of the X-rays used, where the conversion factors were the inverse of the photodiode dosimeter sensitivity. The conversion factors corresponding to the effective energy at the location of each photodiode dosimeter were calculated. A conversion factor corresponding to the X-ray energy incident on the phantom was also obtained, and the system error due to the change in the effective energy was assessed by comparing those conversion factors.

## 3. Results

### 3.1 Confirmation of simulation with measurement

Figure 3 compares the simulated and measured relative doses at each point in the CTDI phantom. Figure 3(a) and 3(b) represent the SECT and DECT scans, respectively. The doses of the CTDI are normalized to unity at the center of the phantom. The result of the simulation is mostly in agreement with the results of the measurements at all the measurement locations. The average percentage difference is about 4.0% for the DECT scan.

### 3.2 Effective energy in anthropomorphic phantom

Figure 4 shows the simulated effective energy at each photodiode dosimeter location during the DECT scan. This result indicates that the effective energy at each point is less than the 71.8 keV of effective energy incident on the phantom. The maximum decrease is about 16% at the location of the liver. The conversion factors were 2.67 for 71.8 keV (incident X-rays) and 2.35 for 59.9 keV (point of maximum energy; liver). The system error of the absorbed dose due to the change in the effective energy was within about 12%.

## 4. Discussion

In a phantom, the effective energy of the X-ray beam would be increased or decreased by several kiloelectron volts. The change is attributed to selective absorption of the low-energy part of the spectrum and Compton scattering in the phantom. Compton scattering radiation approaching each point from other points would decrease the effective energy at each point. The effective energy in each depth of the phantom differs little during a routine SECT scan using a tube voltage 120 kVp (an effective energy of about 50 keV) because the changes in the effective energy attributable to selective absorption and Compton scattering are nearly equal [4]. On the other hand, the effective energy at an X-ray tube voltage of 140 kVp would be decreased by the increase in the contribution from Compton scattering. Figure 4 shows that the effective energies of incident X-rays on points in the bone or on the phantom surface are changed only slightly, and those in soft tissue are further decreased. In soft tissue, the decrease in the effective energy is attributed to the increase in

the scattered X-rays from soft tissue surrounding the dosimeter location. In the points on the phantom surface and in the bone, the effective energy differs little from that of the incident X-rays. These dosimeters would be less affected by scattered X-rays from the phantom.

In dose measurement using DECT with a relatively high tube voltage of 140 kVp, it is possible that a few organ doses are overestimated by 12% because calibration errors could occur due to the X-ray energy dependence of the sensitivity. It is necessary to use the in-phantom dosimetry system carefully for dose measurement to evaluate the radiation dose accurately.

## 5. Conclusions

In a voxel phantom simulation using EGS5, the system errors of the in-phantom dosimetry system due to changes in the effective energies or energy spectrum during DECT were evaluated. The maximum error was about 12% in specific dosimeters installed in soft tissue. It is necessary to consider the characteristics of the dosimeters when using a dosimetry system.

## References

- 1) Aoyama T, Koyama S, and Kawaura C (2002) An in-phantom dosimetry system using pin silicon photodiode radiation sensors for measuring organ doses in x-ray CT and other diagnostic radiology. *Med Phys.* 29, 1504-1510.
- 2) International Commission on Radiological Protection (2007) The 2007 Recommendations of the International Commission on Radiological Protection. ICRP publication 103, *Annals of the ICRP* 37.
- 3) Tucker M, Barnes G, and Chakraborty D. Semiempirical model for generating tungsten target x-ray spectra. *Med Phys.* 18, 211-218 (1991)
- 4) Kondo S, Koyama S. In-phantom beam quality change in X-ray CT: detailed analysis using EGS5. *KEK Proceeding*, 6, 62-67 (2011)

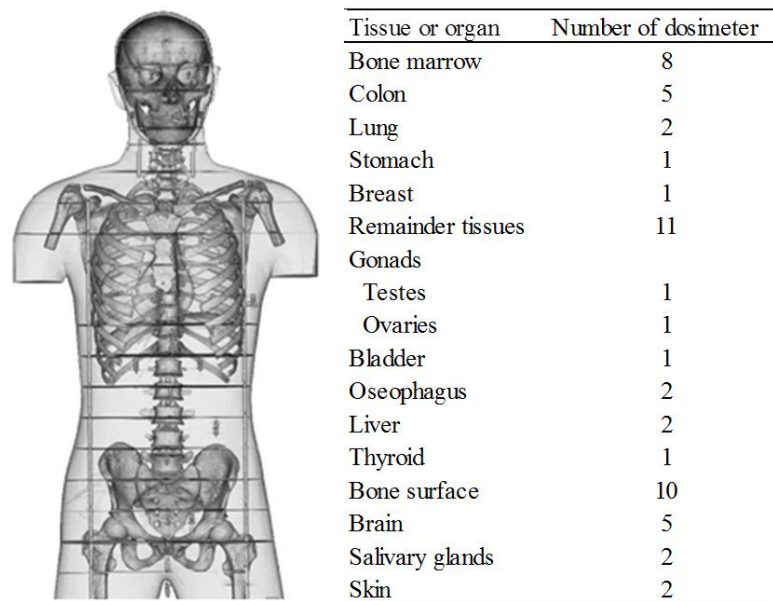


**Figure 1.** Scheme of anthropomorphic phantom used dosimetry system and the number of photodiode X-ray sensors implanted in phantom and each position of tissues and organs.

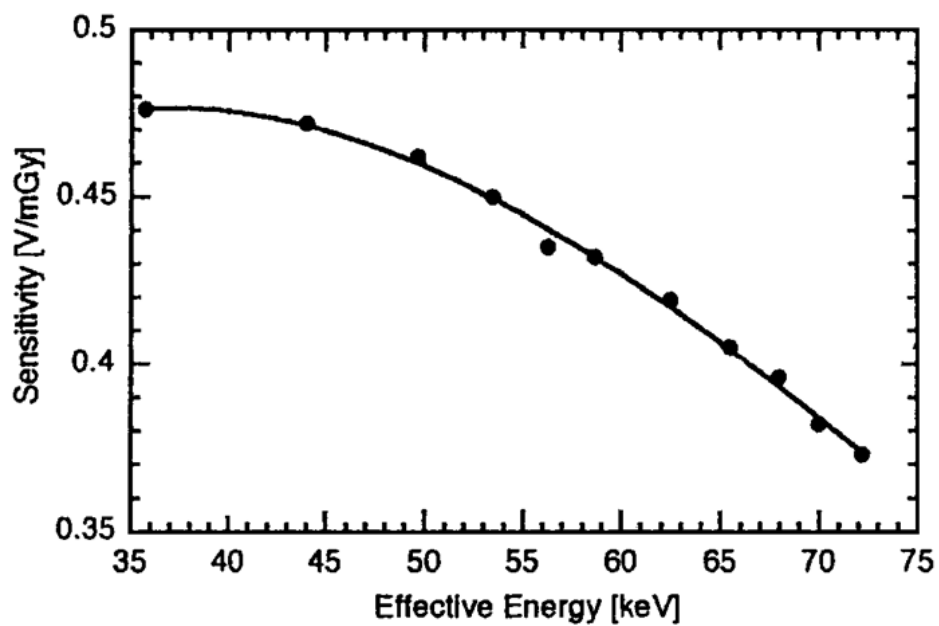


**Figure 2.** X-ray energy dependence of system sensitivity.

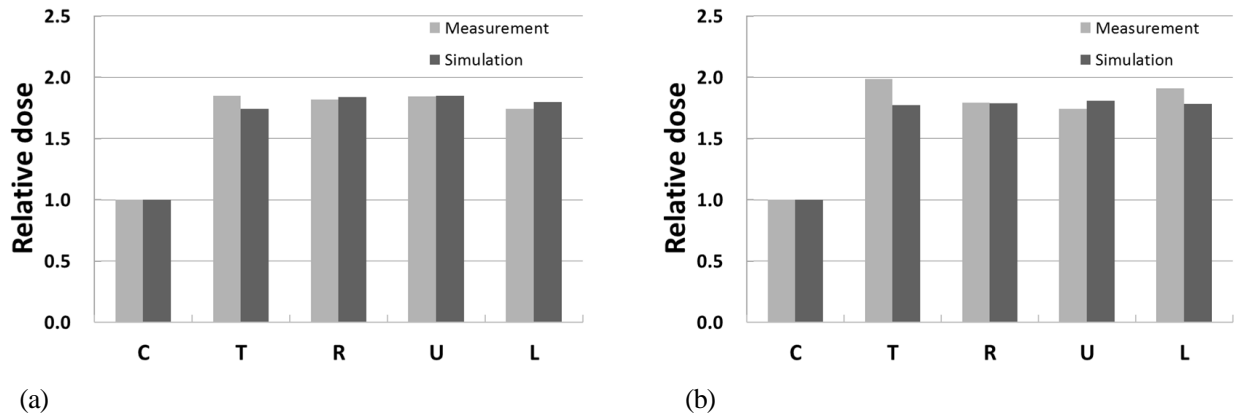


**Figure 3.** Comparison between measured and simulated relative doses at each point in the CTDI phantom with (a) SECT scan and (b) DECT scan, where the doses are normalized to unity at point C, the center of the phantom.

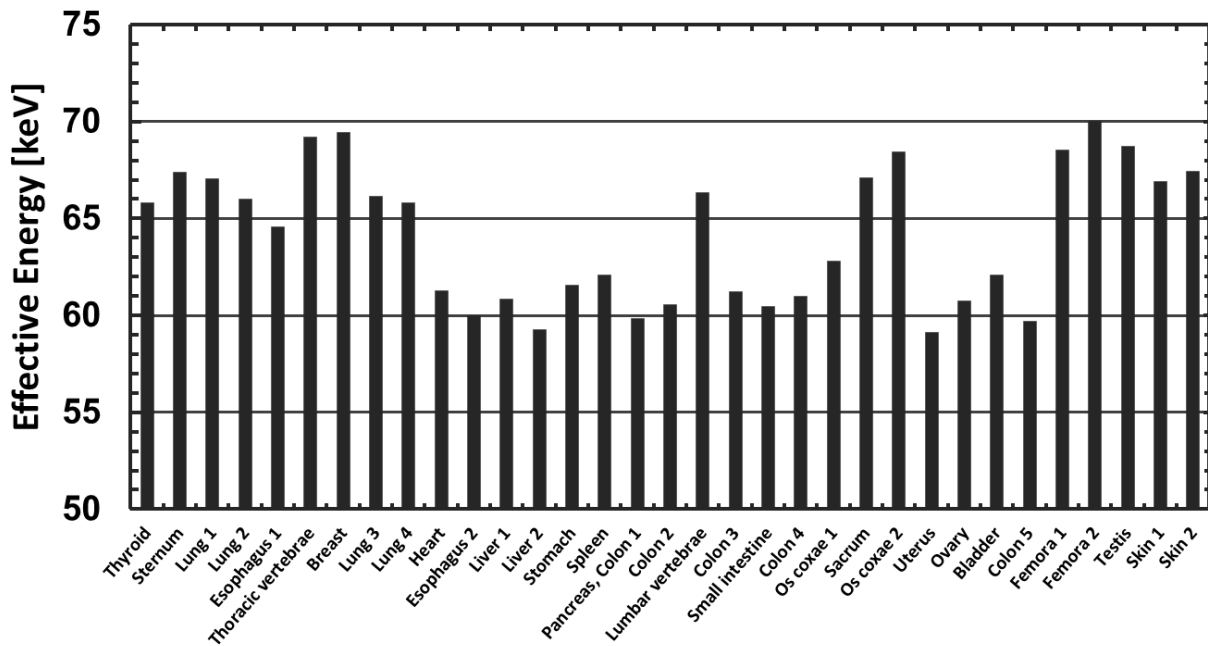


**Figure 4.** Effective energy at each point, where the dosimeters are installed, undergoing a DECT scan for thoracic region.

# QUASI-MONOENERGETIC PHOTON FIELD OF 200 KEV USING A RADIOACTIVE SOURCE WITH BACK-SCATTER LAYOUT

S.M Tajudin, Y.Namito, T.Sanami, H. Hirayama, and H. Iwase

*High Energy Accelerator Research Organization (KEK),*

*1-1 Oho, Tsukuba, Ibaraki 305-0801, Japan*

*E-mail: suffian@post.kek.jp*

## Abstract

We have demonstrated in this paper with Cs-137, a backscattered source with energy of  $\sim 200$  keV could be obtained effectively for radiation detector calibration applications. Vertical arrangements of source and  $1\text{-cm}^3$  CdZnTe detector were tested. Lead block of 10 cm was used to stop the full energy peak of Cs-137. Then we have optimized our backscatter layout to minimize undesirable low energy photons, experimentally. Monte-Carlo simulation (EGS5 code) results reproduced the measurements results well with peaks appearing at correct values around the 200 keV. By considering the backscatter radiation field uniformity both experimentally and theoretically, the optimal backscatter arrangement was obtained for backscatter peak at 189 keV with FWHM of 4.6% (8.7 keV, 14.4ch). Under this condition, we obtained sufficient dose rate of  $5.39\mu\text{Sv/hr}$  for calibration applications with a Cs-137 source intensity of 207.8 MBq.

## 1. Introduction

When ionizing radiation is used in workplaces, around medical X-ray machine, accelerator facility and nuclear reactor, for example, radiation monitors and dosimeters are fundamental tool for control [1, 2]. A detector that could measure all kinds of radiation (particle, energy and intensity) with the same accuracy would be convenient, however no such radiation detector exists. Instead a number of detectors, all with different properties, are used to measure the radiation from different forms. This makes it important to only use the detector for measurements in situations it is designed for [4-6]. In radiation measurements, the sensitivity and detection efficiencies of the detectors are important. Measuring a detector's response at high energy and low energy is essential for detector calibration for accurate photon radiation measurement.

According to the standard procedure by National Institute of Standards and Technology [5], the setup, measurement and procedures for calibration of instruments in terms of air-kerma using gamma-ray from Cs-137 and Co-60 sources. A Cs-137 source is used for standard calibration of gamma-ray dosimeter because it is a stable source and is monoenergetic. However in many cases, we may use these detectors at lower energy ranges. It is useful to calibrate these detectors in low energy region. However there is no stable and monoenergy source for this low energy region except for short half-life source. The closest is Ba-133 with 0.356 MeV, but it produces multi-gamma energy rays of 0.035 MeV (22.6%), 0.081 MeV (34%), 0.303 MeV (18%), 0.356 (62%) and 0.383 MeV (9%).

Instrument calibration often encounters severe problems to perform calibration at a gamma calibration facility. Botter-Jensen and Jensen investigated the effect of scattered gamma ray in the calibration field [7]. This is opposite with our motivation when we aim to use the backscattered radiation field to perform calibration of the dosimeters. We could obtain  $\sim 200$  keV quasi-monoenergetic photon by backscatter layout using Cs-137. We demonstrated here the production of backscattered radiation for  $\sim 200$  keV quasi monoenergetic photon field both experimentally and theoretically by Monte Carlo simulation, EGS5 code [3].

## 2. Materials and Methods

### 2.1 Source

The source used was Cs-137 (Code no: CDC 805) of photon energy 662 keV with 85.1 % branching ratio. It was sealed within an aluminum capsule with source overall dimension was 5 mm diameter x 7 mm length. The source was placed below acrylic window with the inner capsule between two aluminum discs and the overall dimension was 45 mm diameter x 15 mm thickness. The activity of the source was 207.8 MBq (5.61 mCi).

### 2.2 Backscatter layout

The general backscatter layout arrangement used in this study is shown in Figure 1. Specifically, back-scattered photon were measured with CZT detector (KROMEK GR1) whose effective volume is 1 cm x 1 cm x 1 cm. Our goal is to obtain back scattered radiation field uniformly over a wide area. To realize this goal, we needed to optimize several parameters. This layout parameters studied were given in Table 1 and 2:

**Table 1:** Layout arbitrary set parameters.

Layout Variables	Arbitrary parameters
i) Alignment of detector with respect to source	In align with source to obtained high peak ratio
ii) Thickness of Pb block	10 cm as enough to block 662 keV photon
iii) Scattering material	Concrete floor as more practical

**Table 2:** Layout optimized parameters surveyed.

Layout Variables	Optimized parameters
i) Source to floor distance (SFD)	SFD at 20 cm offer highest peak to total ratio as Figure 2
ii) Detector to Pb block distance (DPD)	Investigated for optimum range

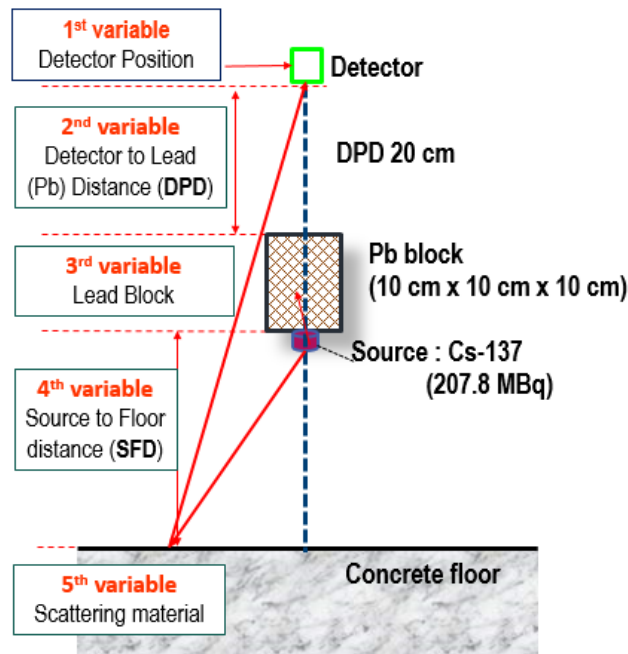


**Figure 1:** Backscatter layout parameters.

Both experiment and calculation used the same vertical geometry. The main focus of the study was to optimize the backscatter layout to obtain quasi monoenergy of 200 keV radiation from Cs-137 source through experiments and calculations.

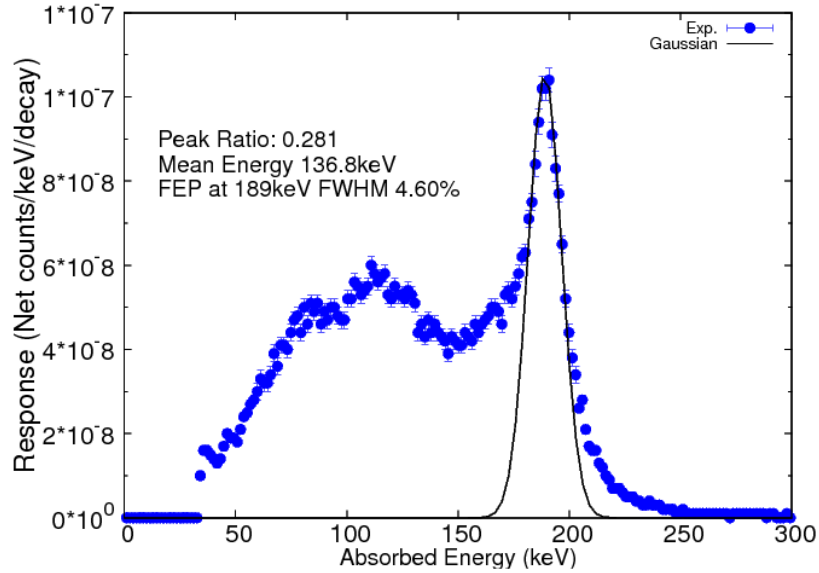


**Figure 2:** Typical measured spectra of ~200 keV by vertical layout.

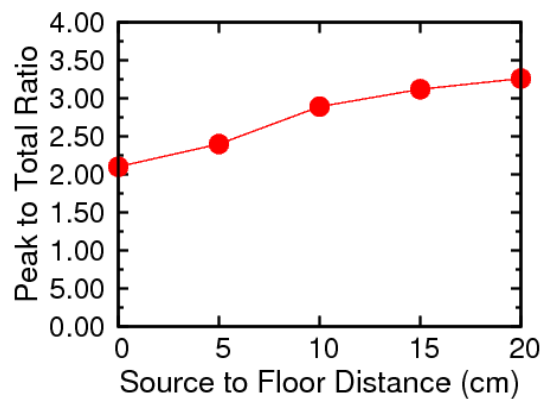
Several indicators were used to study the spectrum that was established as Fig. 2 including the mean energy, the peak to total ratio, and the dose rate ( $\mu\text{Sv/hr}$ ). The mean energy was estimated based on the equation below:

$$\text{Mean energy} = \frac{\sum_{i=1}^n x f(x) dx}{\sum_{i=1}^n f(x) dx} \quad (1)$$

where  $f(x)$  for the net count rate and  $x$  is for energy. Peak to total ratio was estimated as the ratio of integral net counts under the backscatter peak to the total net counts of the whole spectrum.

## 2.3 Optimization Process

### A. Source to Floor Distance (SFD)



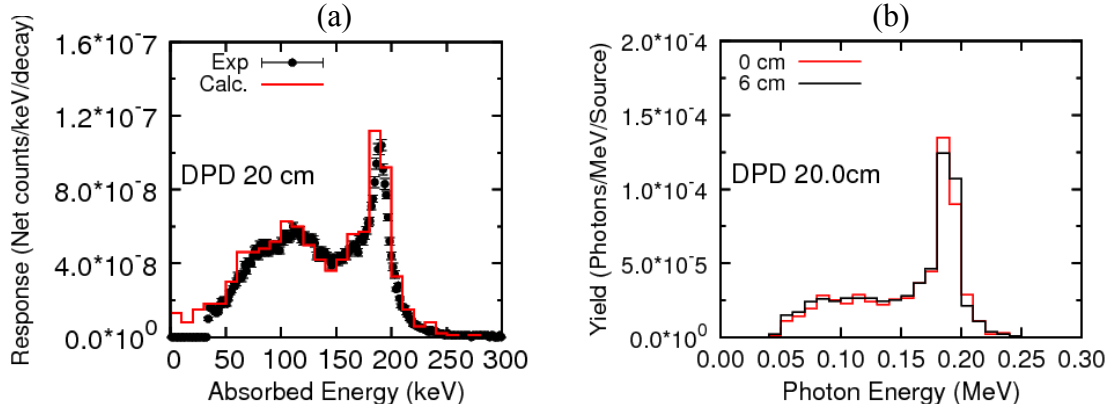
**Figure 3:** Peak-Total ratio as a function of SFD.

Figure 3 shows that the highest peak to total ratio was obtained at a source to floor distance (SFD) 20 cm; where the source is directly under the lead block. Then only the second optimized variable, detector to Pb

distance (DPD) was adjusted (from 10 to 40 cm) while all other parameters remained fixed, as shown in Fig. 1, to obtain a uniform backscattered field.

### B. Effect of DPD: Measured and Calculated Pulse-Height Spectrum of $1\text{cm}^3$ CZT

Figure 4 (a) shows calculated and measured pulse height spectra of DPD 20 cm. The experimental and calculated values are in good agreement as the main peak appears at the correct energy energy; but overestimate the intensity ( $\sim 13\%$ ) at main peaks. Figure 4 (b) shows calculated photon spectra of DPD 20 cm to show the real photon field in this vertical layout regardless the effect of detector used. We calculated for 2 regions; 0 cm meant that the scoring region was aligned with the source, while 6 cm meant that the distance for scoring region was shifted horizontally by a distance of 6 cm.



**Figure 4:** DPD of 20 cm (a) Measured and calculated pulse height spectra (b) Calculated photon spectra.

The effect of DPD were investigated from 10 to 40 cm. The properties of the measured and calculated pulse height distribution spectra were summarized in Table 3 while Table 4 for calculated photon spectra. In Table 3, both values of the measured and calculated for the mean energy and full energy peak energy were accordingly with no significant difference. As average, the calculated peak to total ratio obtained were higher  $\sim 13\%$  than measured. Both measured and calculated pulse height spectra show the same tendency when peak ratio decrease as DPD increased.

**Table 3:** Comparison of measured and calculated pulse height spectra.

DPD (cm)	Mean energy (keV)		Full Energy Peak (keV)		Peak - Total Ratio	
	Exp.	Calc.	Exp.	Calc.	Exp.	Calc.
10	136.5	137.3	188	185	0.299	0.338
20	136.8	137.5	189	190	0.281	0.315
30	136.8	137.4	190	195	0.278	0.318
40	137.4	137.4	195	195	0.269	0.326

**Table 4:** Mean energy, full energy peak and peak to total ratio of photon spectra.

DPD (cm)	Mean energy (keV)		Full Energy Peak (keV)		Peak - Total Ratio	
	0.0 cm	6.0 cm	0.0 cm	6.0 cm	0.0 cm	6.0 cm
10	153.4	153.1	185	185	0.527	0.501
20	155.3	153.6	190	190	0.495	0.482
30	160.5	159.2	195	195	0.470	0.466
40	161.2	162.9	195	195	0.464	0.456

As increasing the DPD, the average energy and main peak of photon energy increased slowly. As shown in Table 4, the higher peak ratio were obtained in case of photon spectra compared to measured or calculated pulse height spectra. The higher intensity for lower energy components as evidenced in Fig. 4 (a) may contributed by multiple scattering effect of the concrete floor and Compton scattering inside the CZT detector.

## 2.4. Confirming Uniformity of the Back-scattered Radiation Field

Establishing uniform radiation field at detector location is important to reduce the position dependence of calibration field, because we may have various size of the detectors. In order to establish a uniform radiation field, the intensity of the backscattered radiation should be sufficient to cover a wider area around the detector. We have examined the field uniformity by checking the distribution of dose rate and spectrum shape both experimentally as well as theoretically. The dose rate uniformity and the spectrum uniformity were investigated with 1 inch NaI(Tl) survey meter (TCS-172B) and 1-cm<sup>3</sup> CZT detector (KROMEK GR1) detector, respectively. These two parameters were examined at different DPD (vertical uniformity) and with respect to horizontal movement of the detector.

### A. DPD and Horizontal Position Dependence of Measured and Calculated Spectrum:

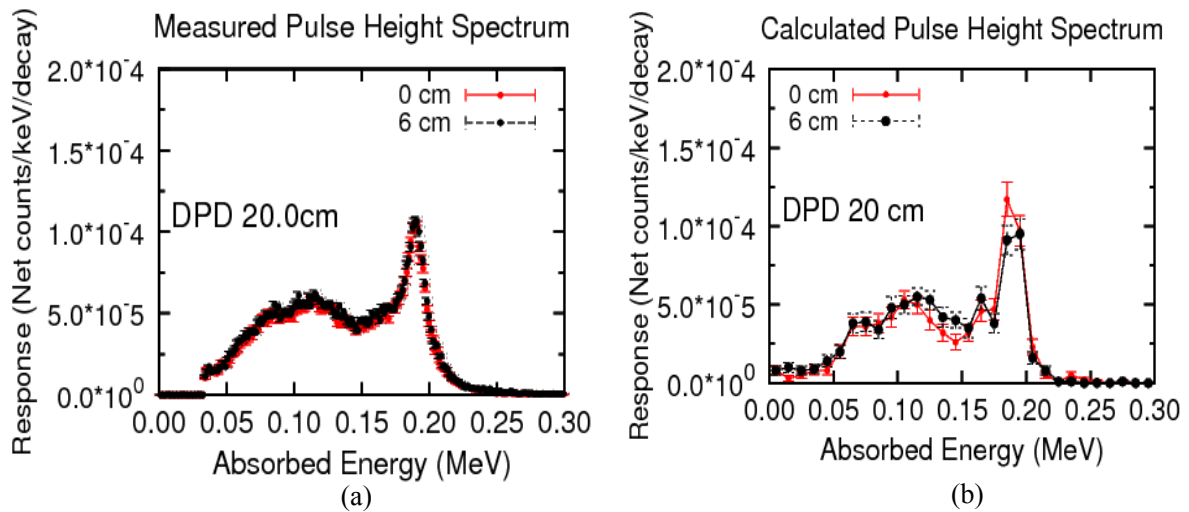


**Figure 5:** The (a) Measured and (b) Calculated pulse height spectra at horizontal of 0 cm and 6 cm for DPD values of 20 cm.

The results for the horizontal spectrum shape dependence are shown in Figure 5. We measured and calculated the pulse height spectrum for two detector horizontal positions; at 0 cm (detector aligned with source or at center) and shifted horizontally by 6 cm. Then the horizontal spectrum checked for every DPD in the range from 10 to 40 cm. We decided on this horizontal distance range (6 cm shifted horizontally) as to suit with our goal to establish calibration field which is adequate to cover various sizes of detectors. The figures show that the spectra shapes were close horizontally in the 20 cm DPD cases.

To determine the amount of spectrum shape changed, we measured the peak to total ratio per 6 cm of horizontal displacement (i.e. the difference in the peak ratio at horizontal displacement of 0 cm and 6 cm) for each DPD cases. A summary was given in Figure 6. The spectrum shape change less than 3% per 6 cm horizontal displacement for the DPD range from 20 to 30 cm. The spectrum shapes at a DPD of 10 cm show a higher percentage change, which is not recommended.

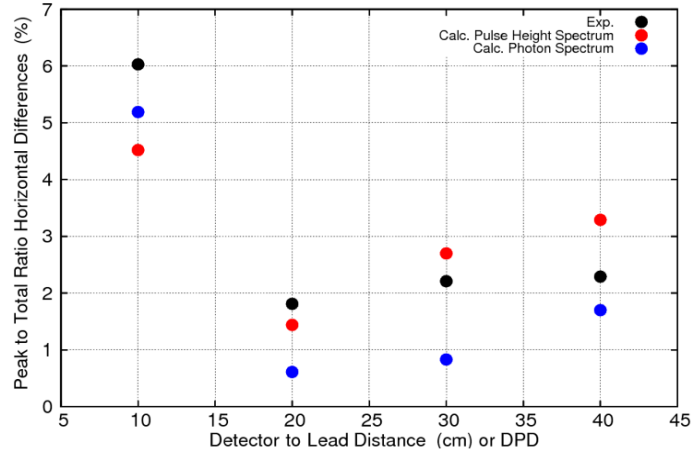


**Figure 6:** Summary the percentage difference of peak ratio for horizontal spectrum shape dependence (per 6 cm) as a function of DPD.

**B. DPD Dependence of Measured and Calculated Spectrum:**

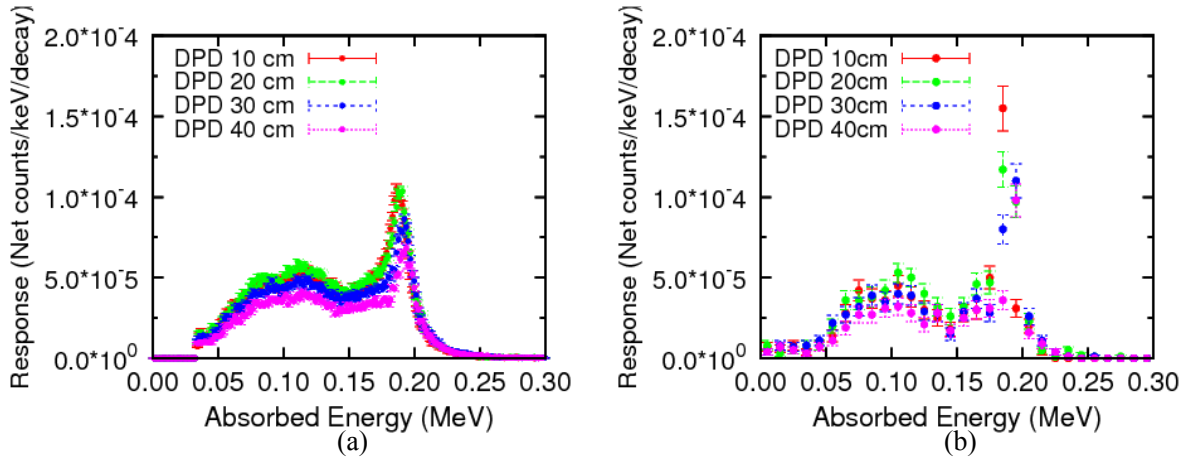


**Figure 7:** Pulse height spectrum: (a) Measured; (b) Calculated.

The measured and calculated vertical uniformities of the pulse height spectra for the different DPDs are shown in Fig. 7. The peak-to-total ratio of the pulse height spectrum slowly decreased as the DPD increased from 10 cm to 40 cm. The peak ratio differences per 10 cm for the vertical spectrum uniformity were measured, and the results are shown in Table 5. The results show that the spectra are more vertically uniform for DPDs from 20 cm to 30 cm with only ~1% variation, as shown by the experimental and calculated data.

**Table 5:** Summary of vertical uniformity of pulse height spectra.

DPD (cm)	Difference of peak ratio at each DPD (%)		Ratio of calculated to experimental	Average difference (%)
	Experimental	Calculated		
20-10	6.41	4.03	0.63	5.22
20-30	1.08	0.72	0.66	0.9
30-40	3.73	2.72	0.72	3.22

Weak dependent of spectrum shape changes for DPD above 20 cm.

**C. Dose Rate for Each Horizontal Position and DPD:**

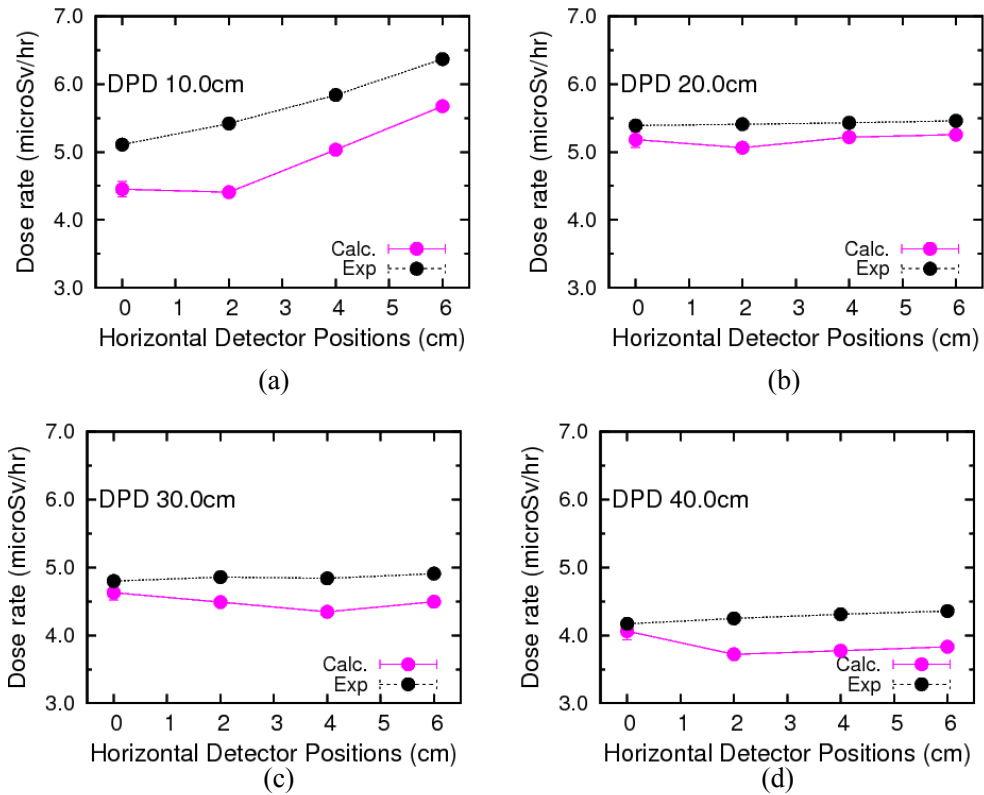


**Figure 8:** Horizontal dose rate distribution for each DPD: (a) 10 cm, (b) 20 cm, (c) 30 cm and (d) 40 cm.

The results for the horizontal dose rate dependence are shown in Figure 8 (a) – (d). The measured and calculated dose rates were obtained every 2 cm (from 0 cm to 6 cm) horizontally, for all DPD cases. As overall, the measured dose rate was slightly higher than calculated dose rate, as measurement value may contain contribution from the nearby buildings or structures at the experiment setup. As our goal to establish wide area of uniform calibration field, we measured the percentage difference of horizontal dose rate distributions per 6 cm, rather than per 2 cm.

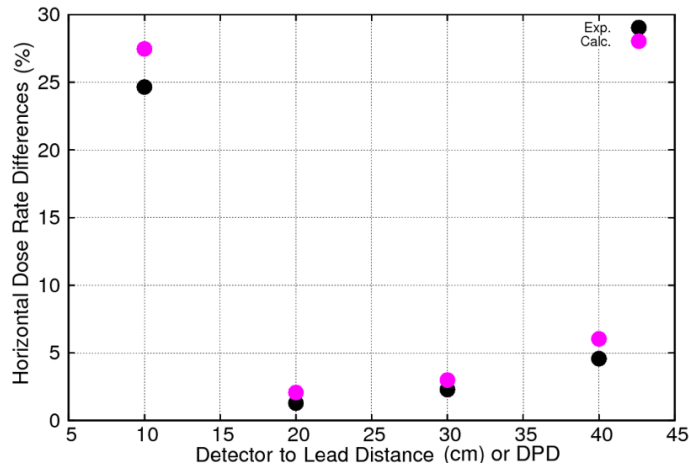


**Figure 9:** Summary of percentage dose rate difference horizontally for each DPD.

The horizontal dose rate differences per 6 cm are summarized in Figure 9. The DPD of 10 cm was not recommended because this plane provided poor horizontal dose rate uniformity. The optimum DPD was 20 to 30 cm range, which gave less than 4% of radiation variation. Anyway, the DPD range could be extended to 40 cm (~5% difference) if the radiation field is too strong for certain detectors.

#### D. DPD Dependence of Dose Rate:

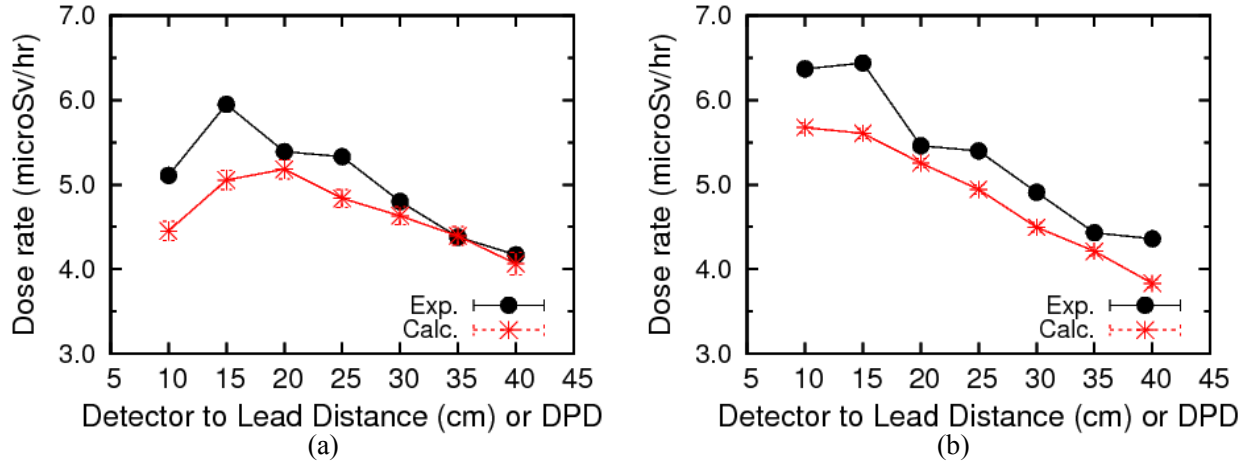


**Figure 10:** Vertical dose rate distribution at (a) 0 cm and (b) 6 cm horizontal displacement.

The measured and calculated vertical dose rate uniformity results are presented in Figure 10. The dose rate were measured for DPD from 10 to 40 cm with 5 cm DPD increment. Figure 10 (a) show the results when the detector was placed at the horizontal 0 cm (aligned with the source) while Figure 10 (b) shows results when the detector was shifted horizontally by 6 cm. The results for both conditions are summarized in Table 6. The table shows the percentage of dose rate difference as DPD increased by 5 cm step. The data show that dose rate depends on DPD weakly, less than 10 % when DPD was above 20 cm.

**Table 6:** Vertical dose rate difference at different DPD ranges.

DPD range (cm)	% dose rate difference per 5 cm (at horiz. 0 cm)		Average difference	% dose rate difference per 5cm (at horiz. 6 cm)		Average difference
	Exp.	Calc.		Exp.	Calc.	
	10 to 15	16.44		13.57	15.00	
15 to 20	9.41	2.51	5.96	15.22	6.25	10.73
20 to 25	1.13	7.09	4.11	1.11	6.33	3.72
25 to 30	9.94	4.51	7.23	9.98	9.95	9.97
30 to 35	8.75	5.11	6.93	9.78	6.32	8.05
35 to 40	4.79	7.51	6.15	1.58	9.01	5.30

### 3. Result

A summary of the established uniform backscattered radiation fields is presented in Table 7.

**Table 7:** Summary of established uniform back-scattered radiation fields.

Parameters	Backscattered radiation field uniformity					Summary of radiation uniformity range		Estimated uniform dose volume established	
	Horizontal (0.0 to 6.0 cm)	Variation		Vertical (10 to 40 cm)	Variation				
CZT spectrum	DPD range 20-30 cm	Exp.	< 3%	DPD above 10 cm	Exp.	< 4%	Horiz.	6 cm	1440 cm <sup>3</sup>
		Calc.			Calc.			< 3%	
Dose rate		Exp.	< 3%	DPD above 10 cm	Exp.	< 10%	Vert.	10 cm	
		Calc.			Calc.			(between DPD 20 to 30 cm)	

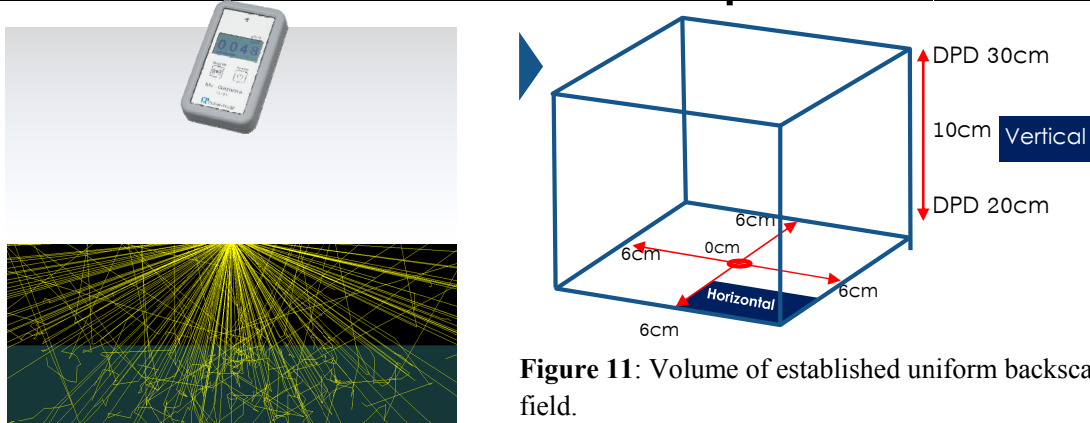


**Figure 11:** Volume of established uniform backscatter field.

In Figure 11, the backscatter field was established uniformly over a wide area. It is important to reduce the detector position dependence of the calibration field.

#### 4. Conclusions

By considering the backscatter radiation field uniformity from experimental data and calculation, the optimal backscatter arrangement is when detector to Pb distances of 20 cm with a source to floor distance of 20 cm. The backscatter peak is at 189 keV FWHM 4.6% (8.7 keV, 14.4ch). We have also demonstrated both experimentally and theoretically that adequate dose rate of 5.39 $\mu$ Sv/hr (background dose rate is 0.066  $\pm$  0.009 $\mu$ Sv/hr) for calibration could be obtained using not so strong source (207.8 MBq) with backscatter layout. We have successfully demonstrated two-energy calibration (~200 keV and 662 keV) to be used for survey meter calibration from a monoenergetic radioactive source (Cs-137). We believe that our method will be very effective for accurate calibration of dosimeters which in turn essential for any instrument.

#### References

1. D Thorelli. Development of Constancy Control and Calibration Protocols for Radiation Monitor Devices and Estimations of Surface Dose Rates from Radioactive Waste Containers Used at University of Gothenburg. Master Thesis, University of Gothenburg, 2008.
2. ANSI N323, American National Standard Radiation Protection Instrumentation Test and Calibration, Portable Survey Instruments. American National Standards Institute. 1997.
3. H. Hirayama, Y. Namito, A. F. Bielajew, S. J. Wilderman and W. R. Nelson, The EGS5 Code System (2010) SLAC Report number: SLAC-R-730; KEK Report number: 2005-8.
4. S.L. Lindbeck, W.H. Steigelmann, E.F. Williams Jr. Calibration for gamma radiation detection instruments Nuclear Engineering and Design, **9**, 311–314 (1969).
5. L. King, MP Unterweger. Radiation detectors calibration. NIST report of calibration, 2009.
6. LH Khiem, N Van Do, PD Khue. Method for detector calibration in radiation measurement of large samples. J. Radioanal. Nucl. Chem., Letters, **200**, 299-304 (1995).
7. L Botter-Jensen, PH Jensen. Determination of scattered gamma radiation in the calibration of environmental dose rate meters. Radiation Protection Dosimetry, **42**, 291-299 (1992).

# CALCULATION OF DOSE RATE DISTRIBUTIONS FOR A RUTHENIUM OPHTHALMIC APPLICATOR

**M. Kato, T. Kurosawa, and N. Saito**

*National Metrology Institute of Japan, National Institute of Advanced Industrial Science and Technology,  
Umezono 1-1-1, Tsukuba, Ibaraki 305-8568, Japan  
e-mail: masahiro-katou@aist.go.jp*

## **Abstract**

Dose rate distributions along the center axis of a Ru-106 ophthalmic applicator and those as a function of position off of the center axis were calculated using the EGS5 code system in order to be compared with calculation results by ACCEPT 3.0 code and reference data provided from the source manufacture. The EGS5 results are in agreement with the reference data. Using this calculation method, we derived two correction factors with a standard uncertainty of 0.8 % required for absorbed dose measurements by a radiochromic film detector.

## **1. Introduction**

National Metrology Institute of Japan (NMIJ) has been developing dose standards for ionizing radiation from brachytherapy sources. A calibration service of an I-125 brachytherapy source started in 2013 while dose standards of Ru-106 and Ir-192 sources are planned to be disseminated in a couple of years. In order to establish the dose standards, a discrepancy between the ideal conditions based on a definition of a quantity and actual conditions of measurement, such as a perturbation of the reference radiation fields by the measurement device, need to be considered. Derivation of a correction factors by a Monte Carlo simulation is a well-known method to correct the discrepancy.

The Ru-106 beta particle sources are widely used as ophthalmic applicators [1]. Accurate dosimetry measurements from the Ru-106 sources have a difficulty because dose rate changes significantly around the point to be measured, so called the reference point, due to the short distance from the source to the reference point, and some of the sources have a concave shape. Two kinds of measurements should be applied for the establishment of the absorbed dose standard of Ru-106 ophthalmic applicators. One is the absorbed dose measurement at the reference point. The reference point for the Ru-106 concave source is specified as 2 mm from the bottom of the curved surface so that large detectors cannot determine the dose rate at the reference point directly. The calibrated radiochromic film is one of the most appropriate detectors for the measurements because they have thin sensitive layer, small energy dependence and tissue equivalence, and can be cut and shape to one's needs [2-4]. The other is a measurement of a dose rate distribution. The dose rate distribution has been studied by experimentally [2-3, 5] and theoretically [3,6]

for more than 20 years.

In this study, depth dose distribution and radial dose distribution for a Ru-106 concave source were compared with calculation results and reference data provided from the source manufacture. The distributions were calculated using the EGS 5 (Electron Gamma shower 5) code system [7] in the present study. We also calculated the dose rate around the reference point in some geometric conditions to derive two correction factors to be used in the radiochromic film measurements for a Ru-106 concave source.

## 2. Materials and Methods

### 2.1 Beta particle source, Ru-106 ophthalmic applicator

The sources in this calculation are the Ru-106 beta particle sources designed as an ophthalmic applicator (Eckert & Ziegler BEBIG, type COC and type CCB). Figure 1 shows the picture and schematic diagram of their cross section. The source is called as a concave source which shape is a part of a spherical surface. The part which is cut out in the COC source seen in Figure 1 (a) was not taken into account in this calculation while the CCB type source doesn't have such a part. The dimensions of the diameter  $D$ , radius  $R$ , and height  $h$  of the sources are provided by the manufacture. Both the sources are made of silver of the 1 mm thickness. The purity of the silver is 0.9999 and the purity is regarded as unity in this simulation. Radioactive ruthenium is uniformly distributed over a depth of 0.1 mm inside the silver. The incident energies of the beta particle for this calculation were determined according to a function reported in ICRU72 [9]. The energy bin of the incident energy was set to 50 keV in this study.

### 2.2 Geometries

In the calculation for the CCB type source, we have defined the geometry to be the same as the reported geometry [6] as possible because the calculation aimed to validate our user codes which define the sources, geometries and scoring conditions for the simulation. Figure 2(a) shows the schematic diagrams of the calculation geometry. A water sphere with a radius of 12.1 mm was placed to be connected with the CCB type source as shown in the figure. Scoring regions in the sphere were defined as rings and cylinders which are shown by the rectangle in figure 2(a). The radius of the cylinders and the width of the rings was 1 mm, and thickness of them was 0.1 mm. Note that the radius of the actual CCB source is 12.0 mm but Cross *et al.* calculated with the value of 12.1 mm.

This geometry for the dose rate calculation in a radiochromic film from the COC type source is shown in Figure 2(b). The source and the radiochromic film (International Specialty Products, GAFCHROMIC® EBT2) were arranged in water or a tough water phantom [10]. The EBT2 film is made by laminating an active layer between non-active layers made of polyester. The physical characters and chemical composition of the tough water phantom and the EBT2 film are obtained from literatures [10,11]. The size of the film was 4.5 mm x 4.5 mm in this calculation. Dose rate at the center of the active layer of the film were calculated for the three conditions which are summarized in Table 1. The diameter and thickness of the region where energy deposit were scored were 4 mm and 0.03 mm, respectively.

### 2.3 Calculation method

The user codes used in this study were reformed codes based on a KEK sample user code, ucphantomcgv.f [12]. The EGS5 code system was run on Cygin with an operating system Windows Vista or Windows 7. The parameter EDEP (energy deposited) was scored for the dose rate calculation. The cutoff energies for

the transport calculation of electron (ECUT) and photon (PCUT) in all calculations were set to 521 keV and 10 keV, respectively. The history number was  $1 \times 10^7$  or  $2 \times 10^7$ . The option parameters were set as default.

### 3. Results and Discussion

#### 3.1 Dose distributions in a water sphere

Figure 3(a) shows the depth dose distributions along the central axis, which are normalized to the dose at 2 mm in depth calculated in this study. The distribution of ACCEPT 3.0 calculation [6] and the reference data provided by the manufacturer are also shown for a comparison. The statistical standard uncertainties of calculating dose rates in this work are less than 1% in depths of 0.5 mm - 4 mm, and less than 4% in 5 mm - 11 mm. Those by Cross *et al* are 1 % or less. The EGS5 and ACCEPT 3.0 results agree with one another within 5% in the depths of 2 mm – 9 mm, while the EGS5 results are in good agreement with the reference data including the short distance region. A comparison between the radial dose distributions in this work and those of Cross *et al*. is shown in Figure 3(b). This figure also shows the differences occurred in the region of the short distance to the source. These differences may arise from the formulation of the concave source and/or dimensions of score region since we cannot reproduce these conditions due to the lack of information. According to the manufacture, since May 2002, Ru-106 applicators have been measured with new detectors with significantly better spatial resolution. The agreement with the reference data based on the more recent method seems to support the validity of the calculation method in this study.

#### 3.2 Correction factors for the radiochromic film measurement

Table 1 shows the dose rate in the active layer of the radiochromic film for the geometry of Figure 2 (b) calculated using the EGS5 code. In order to investigate the effect of the difference of the medium the dose ratio of condition 1 to that of condition 2 was obtained. The value of  $1.016 \pm 0.008$  in column condition 1 is the correction factor to correct the difference between the tough water phantom and water as the medium. The ratio of  $1.032 \pm 0.008$  in column condition 3 is a correction factor to correct the effects of the substance of the film except for the active layer. These correction factors are necessary to derive the absorbed dose to water from the results of the radiochromic film measurement. It seems possible to determine the correction factors in enough accuracy because the standard uncertainty is estimated about 7.5% for radiochromic film measurement from the concave Ru-106 source [5].

### 4. Conclusions

Monte Carlo simulation with the EGS5 code system was performed for the dose rate distributions from the Ru-106 ophthalmic applicator source. The results of the calculation for the depth dose distribution in the water sphere successfully reproduced the reference data provided by the manufacturer. We also calculated the correction factors required for the radiochromic film measurements with enough accuracy. The calculation method validate in this report seems to be useful in the dosimetry measurement from the ophthalmic brachytherapy sources.

## References

- 1) ISO 21439:2009, “Clinical dosimetry – Beta radiation sources for brachytherapy”.
- 2) C. G. Soares, “Calibration of ophthalmic applicators at NIST: A revised approach”, *Med. Phys.* **18**, 787-793 (1991).
- 3) G. Taccini, F. Cavagnetto, G. Coscia, S. Garelli, and A. Pilot, “The determination of dose characteristics of ruthenium ophthalmic applicators using radiochromic film”, *Med. Phys.* **24**, 2034-2037 (1997).
- 4) C. G. Soares, “Radiochromic film dosimetry”, *Radiation Measurements* **41**, S100-S116 (2007).
- 5) C. S. Soares, S. Vynckier, H. Järvinen, W. G. Cross, P. Sipilä, D. Flühs, B. Schaeken, F. A. Mourtada, G. A. Bass, and T. T. Williams, “Dosimetry of beta-ray ophthalmic applicators: Comparison of different measurement methods”, *Med. Phys.* **28**, 1373-1384 (2001).
- 6) W. G. Cross, J. Hokkanen, H. Järvinen, F. Mourtada, P. Sipilä, C. G. Soares, and S. Vynckier, “Calculation of beta-ray dose distributions from ophthalmic applicators and comparison with measurements in a model eye”, *Med. Phys.* **28**, 1385-1396 (2001).
- 7) H. Hirayama, Y. Namito, A.F. Bielajew, S.J. Wilderman and W.R. Nelson, “The EGS5 code System”, SLAC-R-730 (2005).
- 8) J. A. Halbleib, R. P. Kensek, T. A. Mehlhorn, G. D. Valdez, S. M. Seltzer, and M. J. Berger, “ITS Version 3.0: The integrated TIGER Series of Coupled Electron/Photon Monte Carlo Transport Codes”, Report SAND91-1634, Sandia National Laboratories, NM, USA. (1992).
- 9) ICRU Report 72, “Dosimetry of Beta Rays and Low-Energy Photons for Brachytherapy with Sealed Sources”, (Bethesda, MD) 2004.
- 10) T. Fujisaki, T. Hiraoka, H. Saitoh, M. Kimura, A. Kuwabara, H. Muraishi, S. Abe, K. Nishimura, and T. Inada, “Trial production of water substitute phantom considering the effect of light”, *Nippon Acta. Radiologica* **63**, 86-91 (2002), in Japanese
- 11) International Specialty Products, “GAFCHROMIC® EBT2 - Self-Developing film for radiotherapy dosimetry” (2009)
- 12) EGS activities at KEK, <http://rcwww.kek.jp/research/egs/kek/>

**Table 1.** Dose calculation condition and the calculated dose rate with the uncertainty. See also Figure 2 (b).

	Condition 1	Condition 2	Condition 3
Medium	Tough water	Water	Water
Radiochromic film	Active layer and non-sensitive layer	Active layer and non-sensitive layer	Active layer. Nonsensitive layer was replaced by the water
Position of the center of the active layer on z axis	2.0 mm	2.0 mm	2.0 mm
Relative dose rate	8.597	8.463	8.730
Relative uncertainty	0.58 %	0.57 %	0.57 %
Dose ratio to condition 2	1.016 $\pm$ 0.008	-	1.016 $\pm$ 0.008

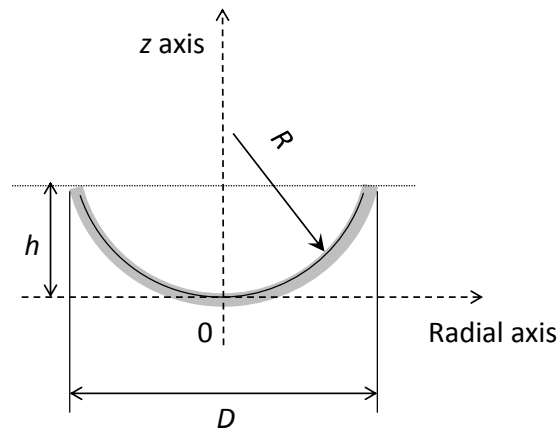


**Figure 1.** Picture of a COC type Ru-106 source (a) and schematic drawing of the cross section (b). The solid curve in the gray colored region in (b) refers to a radioactive layer. Geometric parameters of the CCB and COC type sources are 20.2 mm and 25.4 mm in diameter  $D$ , 12 mm and 14 mm in radius  $R$ , and 5.4 mm and 7.5 mm in height  $h$ , respectively.

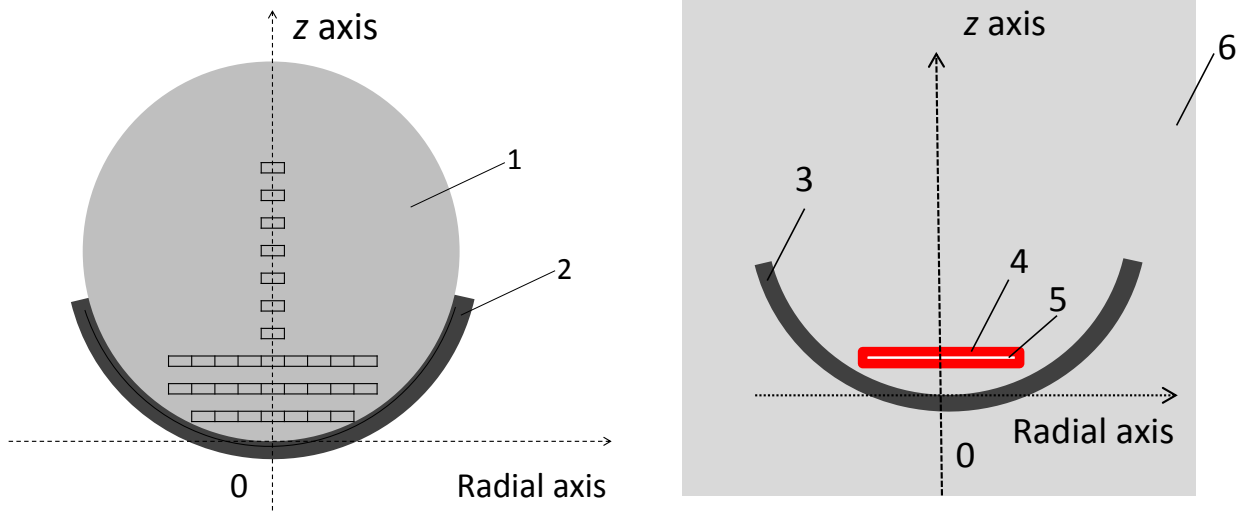


**Figure 2.** Calculation geometries described in the cylindrical coordinate system. (a) CCB type source. 1: water sphere of 12.1 mm which models an eye. 2: ruthenium source type CCB, Regions for the dose rate calculation are shown by the rectangles. (b) COC type source and radiochromic film. 3: ruthenium source type COC, 4: non-sensitive layer of the radiochromic film, 5: active layer of the radiochromic film. 6: a medium which material is water or tough water. Details of the geometric conditions are summarized in Table 1.

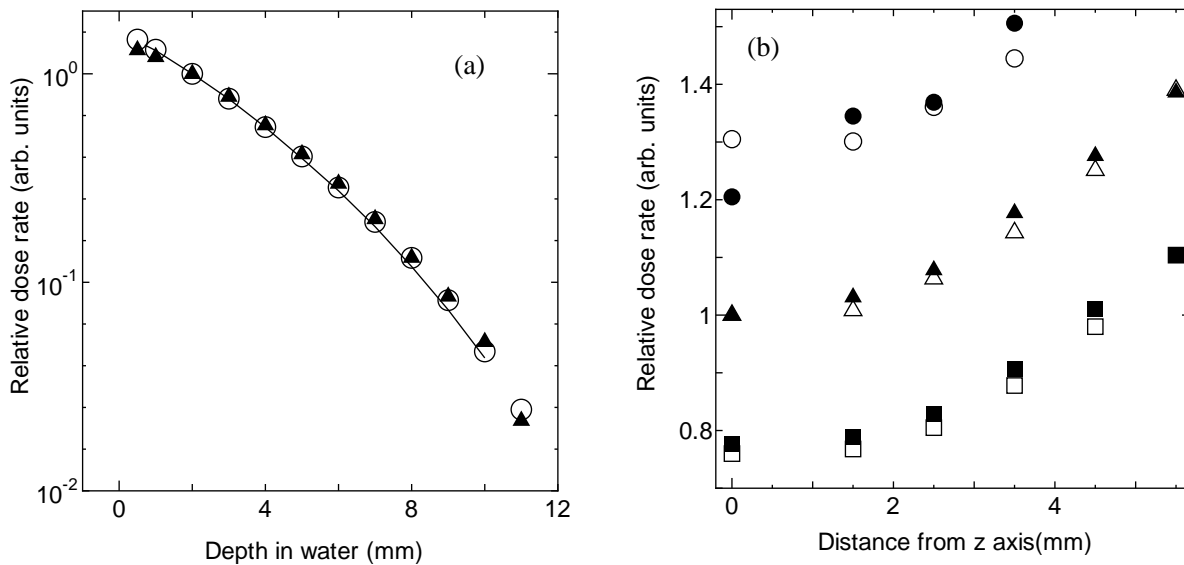


**Figure 3.** Comparisons of the results of Monte Carlo simulations: (a) depth distribution (b) radial distribution. Open symbols: this work (EGS5), solid symbols: Cross *et al* (ACCEPT3.0) and solid curve: reference data provided by the manufacturer. The dose rate was normalized to that on z axis and at 2 mm in depth. In figure 3 (b), circles refer to dose rates at 1 mm in depth, triangles 2 mm and squares 3 mm.

# EFFECT OF THE DIFFERENCE IN ELECTRON CUTOFF ENERGY ON SURFACE DOSE CALCULATION IN THE MONTE CARLO LINEAR ACCELERATOR SIMULATION OF MEGAVOLTAGE PHOTON BEAMS

A. Takeuchi<sup>1</sup>, T. Rachi<sup>2</sup>, R. Yoshida<sup>3</sup>, K. Kojima<sup>4</sup>, M. Niwa<sup>1</sup>, M. Komori<sup>1</sup>, H. Oguchi<sup>1</sup>

<sup>1</sup>*Department of Radiological Sciences, Graduate School of Medicine,  
Nagoya University, Nagoya 461-8673, Japan*

<sup>2</sup>*National Cancer Center Hospital East, Kashiwa 277-8577, Japan*

<sup>3</sup>*Nagoya City University Hospital, Nagoya 467-8602, Japan*

<sup>4</sup>*Yoshikawa Central General Hospital, Yoshikawa 342-0056, Japan  
e-mail: takeuchi.akihiro@f.mbox.nagoya-u.ac.jp*

## Abstract

In the EGS5 codes, there are several user-specified parameters and customized transport algorithms, which may affect the calculation results. In order to fully utilize the Monte Carlo methods in these codes, it is essential to understand all these options and to use them appropriately. In this study, the effects of the electron cutoff energy in EGS5, which are often a trade-off between calculation accuracy and efficiency, were investigated in the buildup region on the depth dose distribution in the water phantom for x-ray in EGS5 user code. The investigated parameters in this study were a value of electron cutoff energy (ECUT) and a value of electron production cutoff energy (AE). The variations in calculated buildup doses were found to be larger than 10% for different cutoff energies. We found that although the choice of a higher AE or ECUT value in the beam modeling can dramatically improve computation efficiency, there is a significant trade-off in surface dose uncertainty. We conclude that nevertheless the dramatically computation efficiency gain, a higher cutoff energy should not be chosen when the surface dose calculations are of dosimetric interest.

## 1. Introduction

For radiation measurement, it has been shown that the direct measurement of radiation dose in the buildup region is difficult using commonly used dosimeters such as ionization chambers, TLDs and radiochromic films and often requires the application of correction factors [1-8]. In addition, radiotherapy treatment planning systems often fail to estimate doses accurately in the buildup region due to limitations in the calculation algorithms [9-12]. For this reason, Monte Carlo (MC) calculations are often referred to as the gold standard for the determination of surface doses [13-15].

The MC method is a powerful tool for accurate radiation dose calculation and is widely used as a benchmark measured doses to different media. The choice of calculation parameter in MC simulation is generally a trade-off between calculation efficiency and accuracy. The user-specified calculation parameters contain the electron cutoff energy. The linear accelerator (linac) geometry of megavoltage photon beams is complicated and has some structures made of heavy metal materials, therefore, MC simulation on the linac requires a long calculation time. Thus, the linac head was set to the high electron cutoff energy for an improvement of calculation efficiency in most cases in MC simulation.

The user-specified electron transport parameters have an effect on the calculation outcome, particularly for complicated geometry calculations in regions which have a high dose gradient such as in the buildup region of

megavoltage photon beams. The photon beams from the linac are contaminated the Compton electrons, and this electron contamination is a contributing factor to the dose in the buildup region. However, in MC simulation the choice of high electron cutoff energy value on the linac head leads to stop the low energy electron transport and to reduce the contaminated electron fluence from the linac head. Therefore, MC calculation with the high electron cutoff energy on the linac head may underestimate the dose in the buildup region.

In this study, we investigate the effect of the difference in electron cutoff energy values on the linac head on calculated surface doses using the Electron Gamma shower version 5 (EGS5) MC code.

## 2. Materials and Methods

### 2.1 Cut off energy in the EGS5

In the EGS5, cut off energy values were set by AE, AP, ECUT and PCUT. AE and AP are parameters that describe the boundary between discrete and continuous energy loss for electrons and gamma rays, respectively. The program will discard particles with energies below these cutoffs, and secondary particles (such as knock on electrons, or bremsstrahlung x-rays) will not be produced. This energy loss is factored into the continuous energy loss if their energy would be below a cutoff energy. ECUT and PCUT are the energies below which electrons and gamma rays are automatically discarded. These are not quite the same as AE and AP, as these parameters have no bearing on whether the program creates a particle, only on whether it is discarded.

### 2.2 The modeling of the linac head

The modeling of the linac from the target to the water phantom was constructed by using CGVIEW with the structural data of Varian Clinac 2100EX of 4 MV and 10 MV x-ray beams. To reduce the calculating time, the phase space file 1 and 2 is used as a variance reduction method. We assumed that the behaviors of photons and electrons through a flattening filter are constant in spite of the motion of jaws and tertiary collimators. Therefore, the phase space file 1 was obtained between the flattening filter and the upper jaws (y-jaws), and additionally the phase space file 2 was obtained on 90 cm from the target. A percentage depth dose (PDD) and off center ratio (OCR) are calculated by using the phase space file 2 data repeatedly to the water phantom placed at 100 cm from the target as the upper surface of the phantom coincided with the isocenter.

Figure 1 shows the created geometry in CGVIEW. Square fields used in this study are from  $5 \times 5 \text{ cm}^2$  to  $30 \times 30 \text{ cm}^2$ . The obtained PDD and OCR are compared with measured values of Clinac 2100EX.

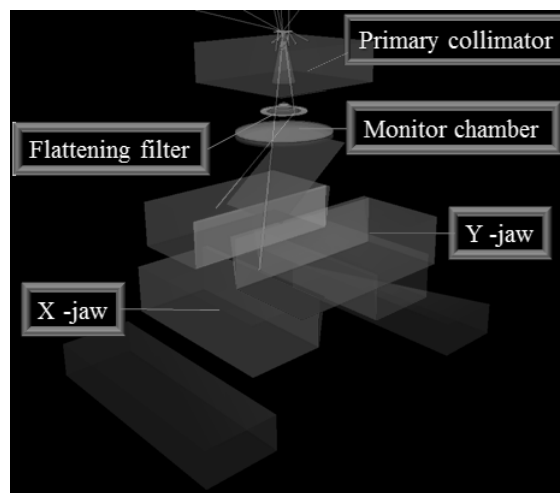


Figure 1. The created geometry in CGVIEW.

### 2.3 Electron fluence calculations

The electron fluence at 90 cm from the target was calculated to investigate the effect of difference in cutoff energy values in the EGS5. An AE value of 0.521 MeV is recommended; however, AE = 0.700 MeV is commonly used for general dose calculations and linac beam modeling since it reduces the computation time significantly. Therefore, for electron fluence calculations, the electron cutoff energy values on the linac were set to ECUT = 0.521 MeV for AE = 0.512 MeV (Reference), ECUT = 0.700 MeV for AE = 0.512 MeV (ECUT = 0.700 MeV), and ECUT = 0.700 MeV for AE = 0.700 MeV (AE = 0.700 MeV). All calculations in this study were performed with a fixed photon cutoff energy PCUT = 0.01 MeV for AP = 0.01 MeV.

### 2.4 Buildup dose calculations in a water phantom

Central axis doses in the buildup region using the phase space file 2 data with the different calculation parameters were calculated in a water phantom. A water phantom size was  $40 \times 40 \times 40 \text{ cm}^3$ , and a total of  $1.6 \times 10^9$  particles were used in order to obtain statistical errors in the calculation of less than 2%. The dose was scored in a voxel with  $2 \times 2 \times 0.05 \text{ mm}^3$  which was used in order to obtain the surface dose of the particularly shallow region in the buildup region. In most MC study, the electron cutoff energy value on a calculation region such as a water phantom is low setting in order to prioritize calculation accuracy over calculation time. In this study, therefore, the electron cutoff energy value of the water region was set to ECUT = 0.521 MeV for AE = 0.521 MeV.

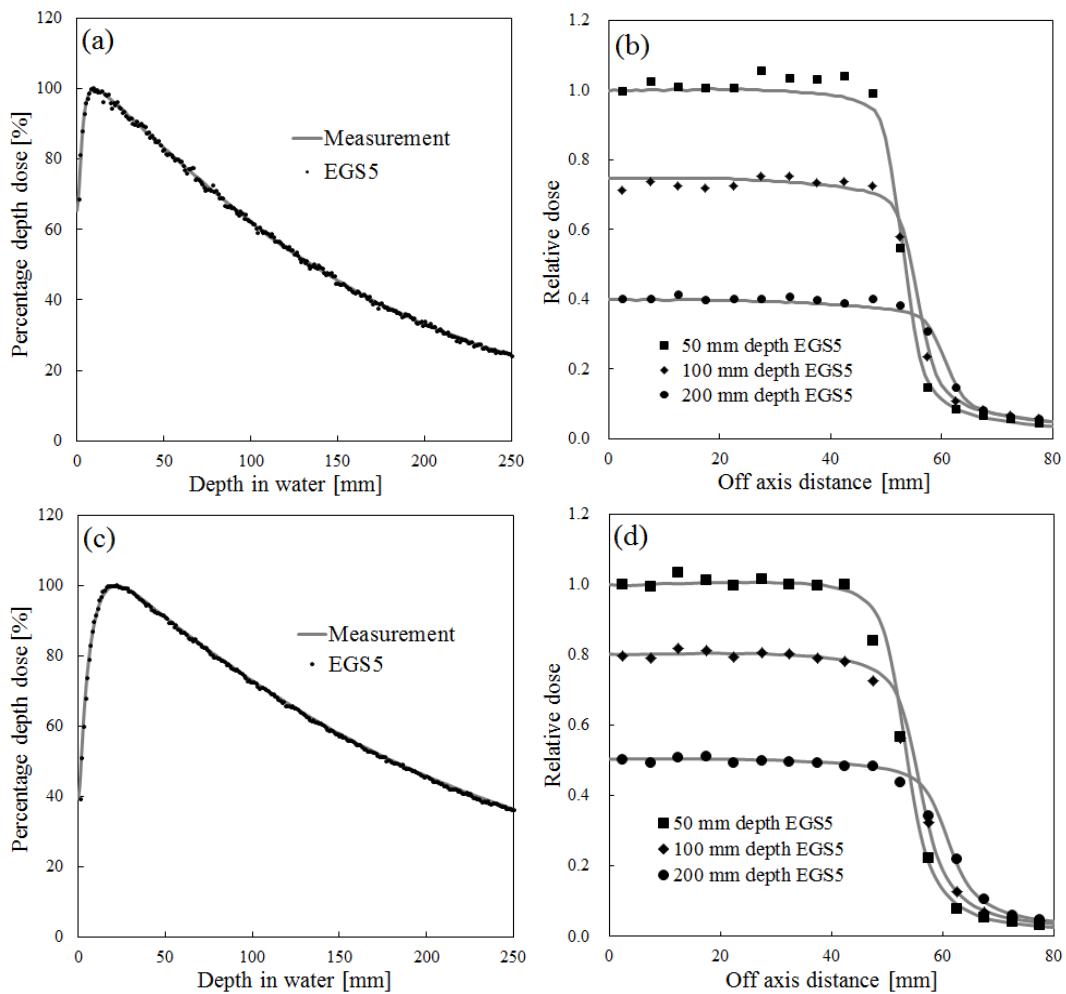


Figure 2. The comparisons of the calculated and measured PDD and OCR in a water phantom for the field size of  $10 \times 10 \text{ cm}^2$ : (a) PDD for 4 MV x-ray, (b) OCR for 4 MV x-ray, (c) PDD for 10 MV x-ray and (d) OCR for 10 MV x-ray.

### 3. Results

#### 3.1 Commissioning validation of the linac model

Figure 2 shows the comparisons of the calculated and measured PDD and OCR in a water phantom for the field size of  $10 \times 10 \text{ cm}^2$  for 4 MV and 10 MV x-ray. The incident electron beam was assumed to have a Gaussian radial intensity distribution. The radial intensity was given by the standard deviation in the Gaussian distribution, here denoted by the full width half maximum (FWHM) value. For conditions of EGS5, a circular cross-section and FWHM value of 4.0 mm and 4.5 mm were used in this simulations for 4 MV and 10 MV x-ray, respectively. The incident electron energy was also assumed to have a Gaussian radial intensity distribution. The mean incident electron energy was 4.50 MeV and 10.47 MeV with FWHM value of 1% and 2.5% of mean incident electron energy for 4 MV and 10 MV x-ray, respectively. As shown in figure 2(a) and 2(c), comparing the calculated and measured PDD, there is a good agreement for most of the calculated doses within 3% and 2% for 4 MV and 10 MV x-ray, respectively. As shown in figure 2(b) and 2(d), comparing the calculated and measured OCR, there is a good agreement for most of the calculated doses within the flattened area for both 4 MV and 10 MV x-ray; however, larger deviations occurred for some points within the penumbra, presumably due to problems in modeling the jaws.

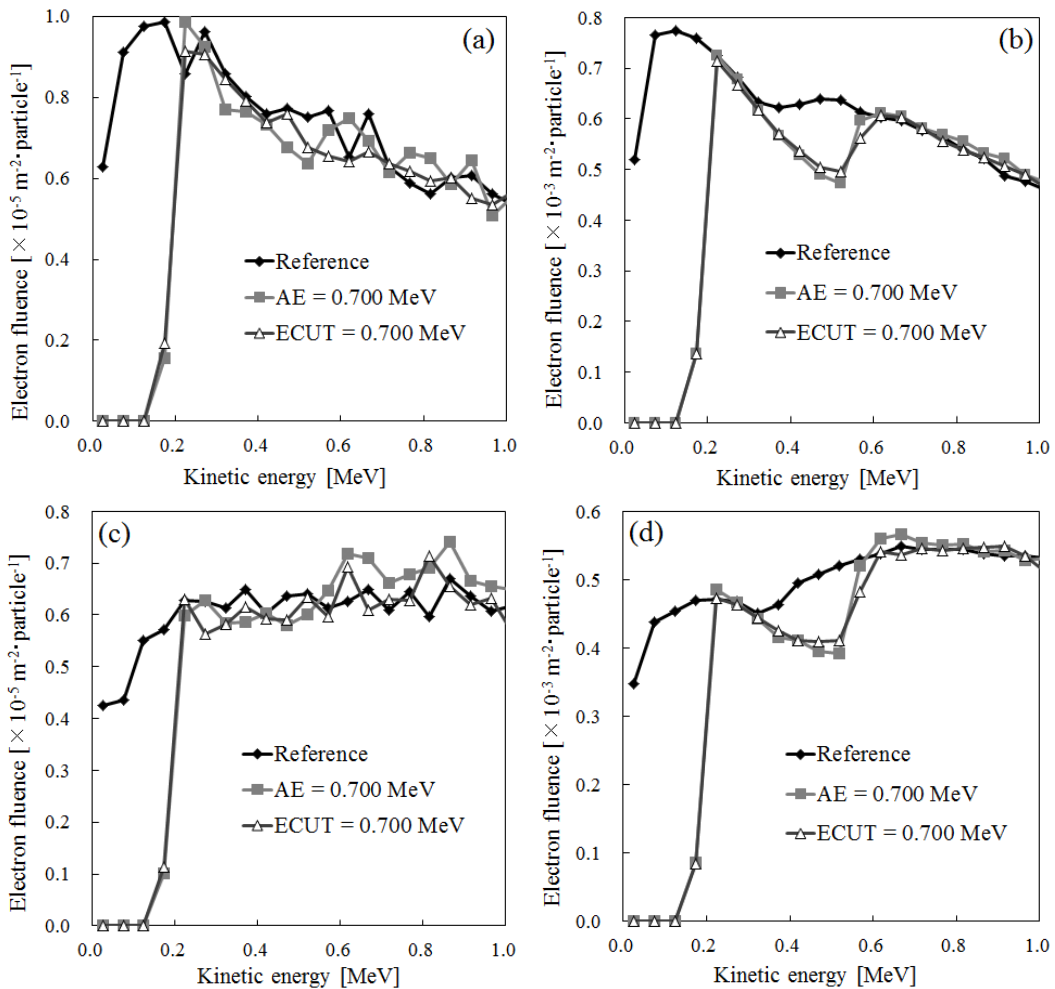


Figure 3. The electron fluence at 90 cm from the target: (a) For the field size of  $5 \times 5 \text{ cm}^2$  for 4 MV x-ray, (b) for the field size of  $30 \times 30 \text{ cm}^2$  for 4 MV x-ray, (c) for the field size of  $5 \times 5 \text{ cm}^2$  for 10 MV x-ray and (d) for the field size of  $30 \times 30 \text{ cm}^2$  for 10 MV x-ray.

The overall agreement of the measured and simulated dose can be considered as accurate, taking the generally requested and the achievable accuracy in radiotherapy into account. The linear accelerator model was therefore accepted as realistic enough for the investigation of the effect of the difference in the cutoff energy on surface dose calculations.

### 3.2 Electron fluence calculations and computation efficiency

Figure 3 shows the electron fluence at 90 cm from the target with the different cutoff energy values for the field size of  $5 \times 5 \text{ cm}^2$  and  $30 \times 30 \text{ cm}^2$  for 4 MV and 10 MV x-ray. It is evident that as the value of ECUT increases, fewer low energy electrons are modeled in EGS5 and stored within the phase space file 2 data for all calculated conditions, while there is virtually no difference in the fluence of electrons with energies above ECUT. However, figure 4 shows there is a significant calculation efficiency gain by using a higher cutoff energy value, resulting in approximately a half of the total CPU time compared to the lower cutoff energy value for AE = 0.700 MeV or ECUT = 0.700 MeV. Significant differences in the electron fluence using a higher AE value of 0.700 MeV as compared to a higher ECUT value of 0.700 MeV are not seen as shown in figure 3.

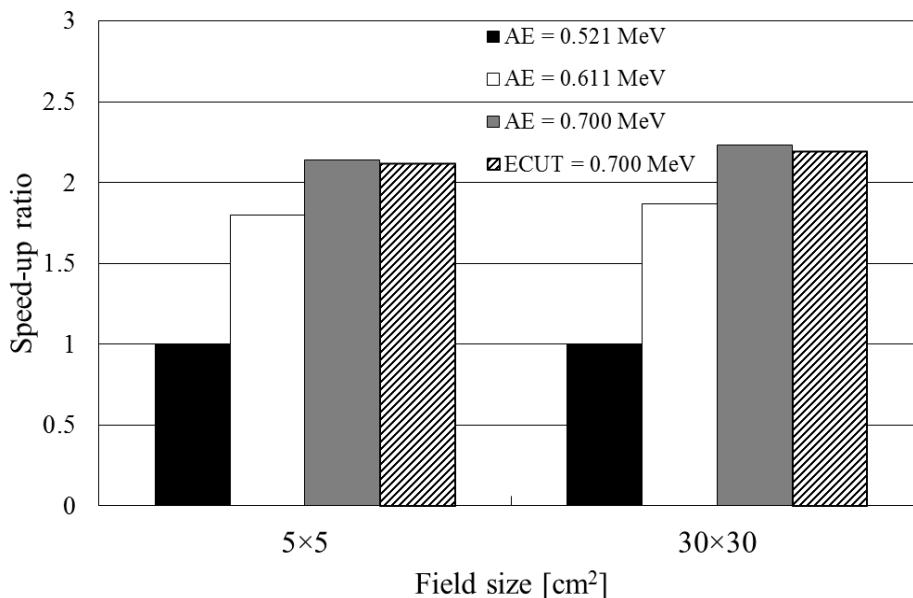


Figure 4. The calculation efficiency gain by changing the AE or ECUT value. The speed-up ratio was defined as the ratio of the calculation time with the reference cutoff energy value divided by the calculation time with an arbitrary cutoff energy value.

### 3.3 Buildup dose calculations in a water phantom

Figure 5 shows the calculated doses in the buildup region with different cutoff energy values for the field size of  $5 \times 5 \text{ cm}^2$  and  $30 \times 30 \text{ cm}^2$  for 4 MV and 10 MV x-ray. From these results, it can be seen that there are large differences in calculated doses in using the different parameters for the field size of  $30 \times 30 \text{ cm}^2$  only; however, the differences in dose decrease gradually with depth.

Figure 5 confirms that using a higher AE value (AE = 0.700 MeV) compared to our reference value (ECUT = 0.521 MeV for AE = 0.521 MeV) in the beam modeling results in a significant underestimation (up to approximately 14% and 7% for 4 MV and 10 MV x-ray, respectively) of the calculated surface dose at depths less than 0.1 mm for the field size of  $30 \times 30 \text{ cm}^2$ . This may be attributed to a deficiency of low energy secondary electrons produced in the linac head that would otherwise be able to reach the water phantom. This is consistent with the electron fluence calculation at the 90 cm from the target, as shown in figure 2. The effect of using the higher ECUT value (ECUT = 0.700 MeV) compared to our reference value shows approximately 11% and 5% underestimation in calculated doses at depths less than 0.1 mm for 4 MV and 10 MV x-ray, respectively. This result showed that when the same parameter value was chosen, the chosen AE value in the dose calculations has a more significant effect than the chosen ECUT value on the calculated doses for depths less than 0.1 mm.

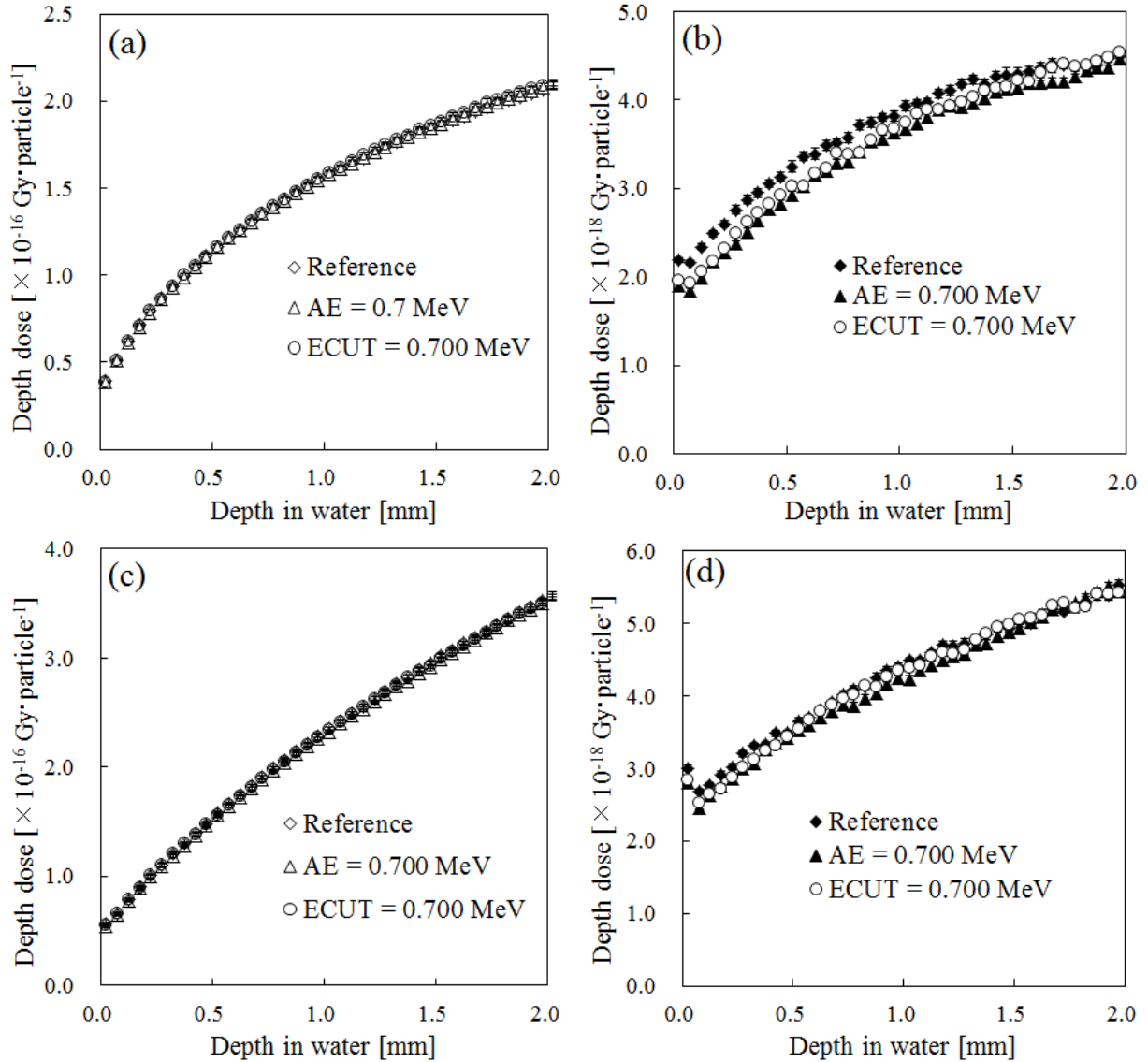


Figure 5. The calculated depth doses in the buildup region: (a) For the field size of  $5 \times 5$  cm $^2$  for 4 MV x-ray, (b) for the field size of  $30 \times 30$  cm $^2$  for 4 MV x-ray, (c) for the field size of  $5 \times 5$  cm $^2$  for 10 MV x-ray and (d) for the field size of  $30 \times 30$  cm $^2$  for 10 MV x-ray.

#### 4. Discussion

Our results demonstrate that using a higher AE or ECUT value in the beam modeling can underestimate build-up doses in a water phantom at depths less than 0.1 mm. This can be attributed to a deficiency of low energy electron contributions to the phantom surface dose. The range of low energy electrons in water is 0.002515 mm for a kinetic energy of 0.010 MeV, while the ranges of relatively higher energy electrons in water are 0.1431 mm for a kinetic energy of 0.100 MeV, and 0.4488 mm for a kinetic energy of 0.200 MeV [16]. According to these ranges data, the lowest AE or ECUT (0.521 MeV, corresponding to a kinetic energy of 0.010 MeV) is required only when doses deposited in micrometer ranges or smaller are of dosimetric interest. However, there is a dramatic efficiency gain in using a higher AE value, reducing the total calculation time by more than half. Notwithstanding the efficiency gain, a higher AE or ECUT should not be chosen when the dose calculations in a water phantom at depths less than 0.1 mm are of dosimetric interest.

## 5. Conclusions

In this work, we investigated the effect on the accuracy and efficiency of surface dose calculations by using different cutoff energies in the EGS5 code. Our results show that there are variations in calculated doses in the buildup region that can reach more than 10% when the cutoff energy was set highly. Nevertheless the dramatically computation efficiency gain, a higher cutoff energy should not be chosen when the surface dose calculations in a water phantom are of dosimetric interest.

## References

- 1) Devic S, Seuntjens J, Abdel-Rahman W, Evans M, Olivares M and Podgorsak E B, "Accurate skin dose measurements using radiochromic film in clinical applications," *Med. Phys.* **33** 1116–24 (2006).
- 2) Stathakis S, Li J S, Paskalev K, Yang J, Wang L and Ma C-M, "Ultra-thin TLDs for skin dose determination in high energy photon beams," *Phys. Med. Biol.* **51** 3549–67 (2006).
- 3) Xiang H F, Song J S, Chin D W H, Cormack R A, Tishler R B, Makrigrigorgos G M, Court L E and Chin L M, "Build-up and surface dose measurements on phantoms using micro-MOSFET in 6 and 10 MV x-ray beams and comparisons with Monte Carlo calculations," *Med. Phys.* **34** 1266–73 (2007).
- 4) Hsu S H, Roberson P L, Chen Y, Marsh R B, Pierce L J and Moran J M, "Assessment of skin dose for breast chest wall radiotherapy as a function of bolus material," *Phys. Med. Biol.* **53** 2593–606 (2008).
- 5) Saibishkumar E P, Mackenzie M A, Severin D, Mihai A, Hanson J, Daly H, Fallone G, Parliament M B and Abdulkarim B S, "Skin-sparing radiation using intensity-modulated radiotherapy after conservative surgery in early-stage breast cancer: a planning study," *Int. J. Radiat. Oncol. Biol. Phys.* **70** 485–91 (2008).
- 6) Zibold F, Sterzing F, Sroka-Perez G, Schubert K, Wagenknecht K, Major G, Debus J and Herfarth K, "Surface dose in the treatment of breast cancer with helical tomotherapy," *Strahlenther. Onkol.* **185** 574–81 (2009).
- 7) Chiu-Tsao S T and Chan M F, "Evaluation of two-dimensional bolus effect of immobilization/support devices on skin doses: a radiochromic EBT film dosimetry study in phantom," *Med. Phys.* **37** 3611–20 (2010).
- 8) Kelly A, Hardcastle N, Metcalfe P, Cutajar D, Quinn A, Foo K, Cardoso M, Barlin S and Rosenfeld A, "Surface dosimetry for breast radiotherapy in the presence of immobilization cast material," *Phys. Med. Biol.* **56** 1001–13 (2011).
- 9) Fogliata A, Vanetti E, Albers D, Brink C, Clivio A, Knoos T, Nicolini Gand Cozzi L, "On the dosimetric behavior of photon dose calculation algorithms in the presence of simple geometric heterogeneities: comparison with Monte Carlo calculations," *Phys. Med. Biol.* **52** 1363–85 (2007).
- 10) Fogliata A, Nicolini G, Vanetti E, Clivio A, Winkler P and Cozzi L, "The impact of photon dose calculation algorithms on expected dose distributions in lungs under different respiratory phases," *Phys. Med. Biol.* **53** 2375–90 (2008).
- 11) Panettieri V, Barsoum P, Westermarck M, Brualla L and Lax I, "AAA and PBC calculation accuracy in the surface build-up region in tangential beam treatments. Phantom and breast case study with the Monte Carlo code PENELOPE," *Radiother. Oncol.* **93** 94–101 (2009).
- 12) Hsu S-H, Moran J M, Chen Y, Kulasekere R and Roberson P L, "Dose discrepancies in the buildup region and their impact on dose calculations for IMRT fields," *Med. Phys.* **37** 2043–53 (2010).
- 13) Abdel-Rahman W, Seuntjens J P, Verhaegen F, Deblois F and Podgorsak E B, "Validation of Monte Carlo calculated surface doses for megavoltage photon beams," *Med. Phys.* **32** 286–98 (2005).
- 14) Rogers D W O, "Fifty years of Monte Carlo simulations for medical physics," *Phys. Med. Biol.* **51** R287–301 (2006).
- 15) Reynaert N, Van der Marck S C, Schaart D R, Van der Zee W, Van Vliet-Vroegindeweij C, Tomsej M, Jansen J, Heijmen B, Coghe M and De Wagter C, "Monte Carlo treatment planning for photon and electron beams," *Radiat. Phys. Chem.* **76** 643–86 (2007).
- 16) NIST DATABASE at [http://physics.nist.gov/cgi-bin/Star/e\\_table.pl](http://physics.nist.gov/cgi-bin/Star/e_table.pl)

# EVALUATION OF S VALUES OF $^{99m}\text{Tc}$ FOR MULTI-REGION MODELS OF KIDNEYS IN THE ICRP VOXEL PHANTOMS

S. Hato<sup>1,2</sup> and S. Kinase<sup>1</sup>

<sup>1</sup>*Ibaraki University, Ibaraki 310-8512, Japan*

<sup>2</sup>*Visible Information Center, Inc. Ibaraki 319-1112, Japan*

*e-mail: hato@vic.co.jp*

## Abstract

The International Commission on Radiological Protection (ICRP) has developed the computational phantoms of the adult Reference Male and Reference Female in ICRP Publication 110. The phantoms are based on medical image data of real people and are constructed as voxel models. Kidneys of the phantoms have been represented as multi-region models (cortex, medulla and pelvis), while in the Medical Internal Radiation Dose Committee kidneys of traditional mathematical phantoms have been expressed as single-region models. In the present study, an impact to internal dose assessments for kidneys of the ICRP voxel phantoms between multi-region and single-region models was revealed by evaluating specific absorbed fractions (SAFs) for photons and electrons and S values of non-uniformly distributed  $^{99m}\text{Tc}$  in the kidneys. It was found that self-irradiation SAFs for the pelvis of the multi-region models are much larger than those of other target/source regions in the kidneys. Self-irradiation S values of  $^{99m}\text{Tc}$  in the pelvis of the multi-region models were also found to be about 14 times higher than that in kidneys of the single-region models. Hence, for non-uniformly distributed  $^{99m}\text{Tc}$  in the kidneys, the multi-region models are suitable for internal dose assessments.

## 1. Introduction

Computational phantoms simulating human body are used to evaluate the energy deposition in organs resulting from internal radiation exposures. Previously, the phantoms have been based upon mathematical expressions described the shape and position of idealized body organs. The phantoms (mathematical phantoms) have been developed by the Medical Internal Radiation Dose (MIRD) Committee [1]. In recent years, computational voxel phantoms for the adult Reference Male and Reference Female have been developed by the International Commission on Radiological Protection (ICRP) [2] to obtain a more realistic replication of human anatomy - ICRP voxel phantoms.

Kidneys of the ICRP voxel phantoms have been represented as multi-region models (cortex, medulla and pelvis), while kidneys of traditional mathematical phantoms have consisted of single-region models. Since the kidneys are seen to concentrate radioactivity non-uniformly, internal dose assessments for radioactivity in the kidneys may be appropriate by multi-region models, rather than by single-region models.

In the present study, an impact to internal dose assessments for multi-region and single-region models of kidneys in the ICRP voxel phantoms was revealed by evaluating specific absorbed fractions (SAFs) of photons and electrons and S values of  $^{99m}\text{Tc}$ , which is widely used in nuclear medicine. Specific absorbed fractions of photons were evaluated using a Monte Carlo code EGS [3] and SAFs of electrons were calculated using a simple assumption – electrons are entirely absorbed in source region. S values of  $^{99m}\text{Tc}$  in the kidneys were evaluated using their SAFs.

## 2. Materials and Methods

### 2.1. Multi-region models of kidneys

The ICRP adult male and female reference voxel phantoms were used in the present study. The voxel sizes are  $2.137 \times 2.137 \times 8.0 \text{ mm}^3$  for the adult male voxel phantom and  $1.775 \times 1.775 \times 4.84 \text{ mm}^3$  for the adult female voxel phantom. Many organs and tissues are segmented and identified. Three regions are segmented in each kidney: cortex, medulla and pelvis. The density and mass of each kidney region in the ICRP voxel phantoms are shown in Table 1.

### 2.2. Evaluation of specific absorption fractions

Specific absorbed fractions (SAFs) for radiation energy  $E_i$  from source region ( $r_s$ ) to target region ( $r_T$ ) is equation (1) with absorption fractions (AFs) and mass of target region ( $M_T$ ).

$$\text{SAF}(r_T \leftarrow r_S; E_i) = \frac{\text{AF}(r_T \leftarrow r_S; E_i)}{M_T} \quad (1)$$

Absorbed fractions (AFs) of photons were evaluated for the kidney models in the ICRP voxel phantoms using a Monte Carlo code, EGS4[3], in conjunction with an EGS4 user code, UCSAF[4]. In the EGS4-UCSAF code, the radiation transport of electrons, positrons and photons in the phantoms was simulated, and correlations between primary and secondary particles are included. The sources of photons were assumed to be uniformly distributed in the source region. The source regions were cortex, medulla and pelvis in the kidneys. Photon histories were selected to be numbers sufficient to reduce statistical uncertainties below 5%. The cut-off energies were set to 1keV for the photons. Absorbed fractions (AFs) of electrons were calculated using a simple assumption -electrons are entirely absorbed into the source region.

### 2.3. Evaluation of S values

S value from source region ( $r_S$ ) to target region ( $r_T$ ) per nuclear transformation of a given radionuclide is evaluated as equation (2) with SAFs, energy ( $E_i$ ) and yield ( $Y_i$ ) of radiations.

$$S(r_T \leftarrow r_S) = \sum_i Y_i E_i \text{SAF}(r_T \leftarrow r_S; E_i) \quad (2)$$

S values of  $^{99m}\text{Tc}$  in the kidneys were evaluated with the SAFs evaluated in the present study and decay data of  $^{99m}\text{Tc}$  [5] (table 2).

## 3. Results and discussion

### 3.1. Specific absorption fractions for multi-region models of kidneys

Specific absorption fractions (SAFs) of photons for multi-region and single-region models of the kidneys in the ICRP voxel phantoms are shown in figure 1. The self-irradiation SAFs for the pelvis (Kidneys-P→Kidneys-P) in the multi-region models at low photon energy is about 15 times higher than that of kidneys (Kidneys→Kidneys) in the single-region models. Specific absorption fractions of electrons for multi-regions and single-region models of the kidneys in the ICRP voxel phantoms are shown in figure 2. The self-irradiation SAFs for the pelvis (Kidneys-P→Kidneys-P) in the multi-region models is about 20 times higher than that of kidneys (Kidneys→Kidneys) in the single-region models.

This fact indicates that the self-irradiation SAFs for the pelvis are larger than those of other target/source regions. These are due to the different mass of target/source regions- mass dependence.

### 3.2. S values of $^{99m}\text{Tc}$ for multi-region models of kidneys

S values of  $^{99m}\text{Tc}$  for multi-region and single-region models of the kidneys in the ICRP voxel phantoms are shown in figure 3. For self-irradiations, the S value of electrons makes a large contribution to the total S value. The self-irradiation S values of  $^{99m}\text{Tc}$  for the pelvis (Kidneys-P→Kidneys-P) in the multi-region models are about 14 times higher than those for kidneys (Kidneys→Kidneys) in the single-region models.

Self-irradiation S values of  $^{99m}\text{Tc}$  in the pelvis are larger than those of other target/source regions.

### 3.3. Comparison of S values of $^{99m}\text{Tc}$ between adult male and female

Comparisons of S values of  $^{99m}\text{Tc}$  in the kidneys between adult male and female are shown in figure 4. The S values for female are slightly larger than that for male. For comparisons, S values of  $^{99m}\text{Tc}$  for the MIRD adult mathematical phantom [6] are also shown in the figure. The S values of  $^{99m}\text{Tc}$  in the kidneys for the ICRP adult male and female voxel phantoms are comparable with those for the MIRD adult mathematical phantom.

## 4. Conclusions

Specific absorbed fractions for the multi-region and single-region models of kidneys in the ICRP voxel phantoms were evaluated using Monte Carlo simulations. S values of  $^{99m}\text{Tc}$  in the kidneys were evaluated combining the SAFs and decay data of ICRP. It was found that the self-irradiation S values of  $^{99m}\text{Tc}$  for single-region models of kidneys are smaller than those for multi-region models of kidneys. The multi-region models are suitable for internal dose assessments for the kidneys.

## References

- 1) W. S. Snyder, M. R. Ford and G. G. Warner, “Estimates of specific absorbed fractions for monoenergetic photon sources uniformly distributed in various organs of a heterogeneous phantoms”, Society of Nuclear Medicine; Medical Internal Radiation Dose Committee Pamphlet, No.5, Revised, New York, NY (1978).
- 2) ICRP, “Adult reference computational phantoms”, ICRP Publication 110, Ann. ICRP 39 (2) (2009).
- 3) W. R. Nelson, H. Hirayama and D. W. O. Rogers, “The EGS4 code system”, SLAC-265, Stanford Linear Accelerator Center, Stanford, CA (1985).
- 4) S. Kinase, M. Zankl, J. Kuwabara, K. Sato, H. Noguchi, J. Funabiki and K. Saito, “Evaluation of specific absorbed fractions in voxel phantoms using Monte Carlo simulation”, Radiat. Prot. Dosim., 105, 557-563 (2003).

- 5) ICRP, “Nuclear decay data for dosimetric calculations”, ICRP Publication 107, Ann. ICRP 38 (3) (2008).
- 6) Lionel G. Bouchet, Wesley E. Bolch, H. Pablo Blanco, Barry W. Wessels, Jeffrey A. Siegel, Didier A. Rajon, Isabelle Clairand and George Sgouros, “MIRD Pamphlet No.19: Absorbed fractions and radionuclide S values for six age-dependent multiregion models of the kidney”, J. Nucl. Med Vol.44, No.7 (2003).

Table 1 Density and mass for multi-region models of kidneys in the ICRP voxel phantoms [2]

Region	Density [g/cm <sup>3</sup> ]	Mass [g]	
		Male	Female
Kidney, left, cortex		107.12	104.63
Kidney, left, medulla	1.050	38.25	37.37
Kidney, left, pelvis		7.63	7.48
Kidney, right, cortex		109.92	87.87
Kidney, right, medulla	1.050	39.25	31.38
Kidney, right, pelvis		7.87	6.28

Table 2 Summary of radiation emissions for <sup>99m</sup>Tc [5]

Radiations	Yield	Energy
	[/nuclear transformation]	[MeV/nuclear transformation]
Gamma rays	8.908×10 <sup>-1</sup>	1.252×10 <sup>-1</sup>
X rays	5.576×10 <sup>0</sup>	1.432×10 <sup>-3</sup>
Beta-	3.700×10 <sup>-5</sup>	4.198×10 <sup>-6</sup>
IC electrons	1.102×10 <sup>0</sup>	1.524×10 <sup>-2</sup>
Auger electrons	4.414×10 <sup>0</sup>	9.397×10 <sup>-4</sup>

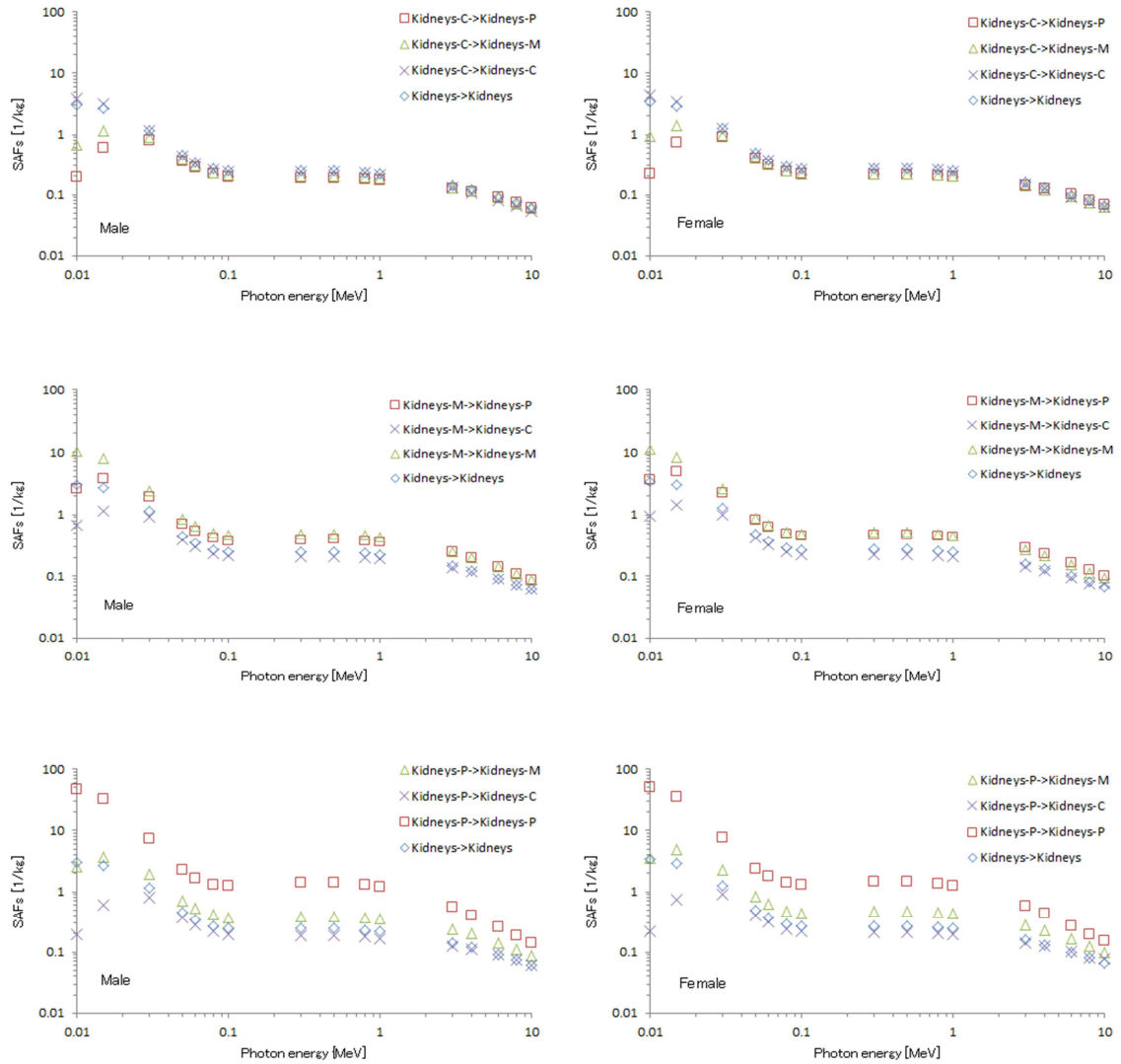


Figure 1. Specific absorbed fractions (SAFs) of photons for kidneys in the ICRP adult male and female voxel phantoms. (Kidneys-C is cortex region of Kidneys. Kidneys-M is medulla region of Kidneys. Kidneys-P is pelvis region of Kidneys. Kidneys is single-region model.)

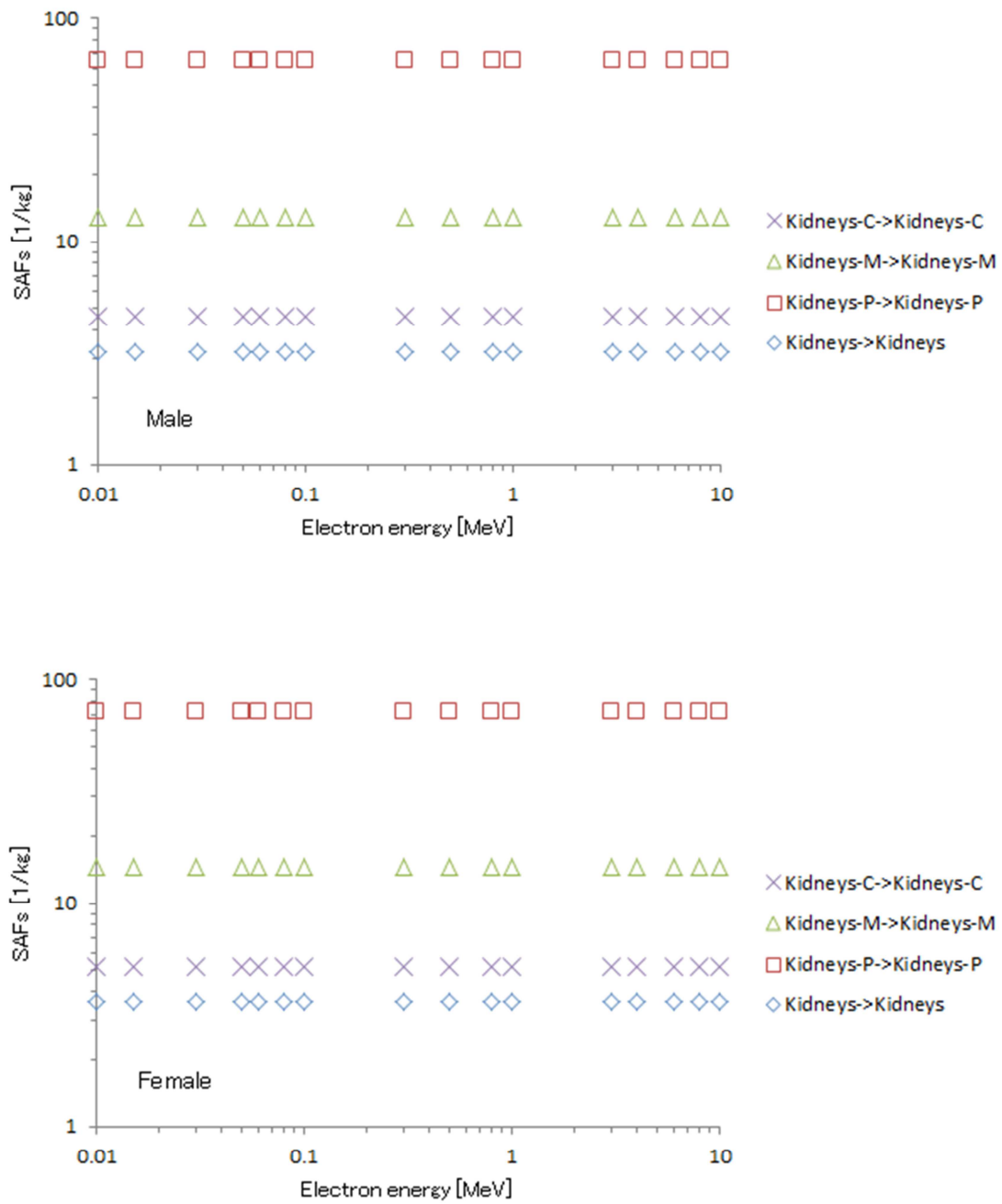


Figure 2. Specific absorbed fractions (SAFs) of electrons for kidneys in the ICRP adult male and female voxel phantoms.

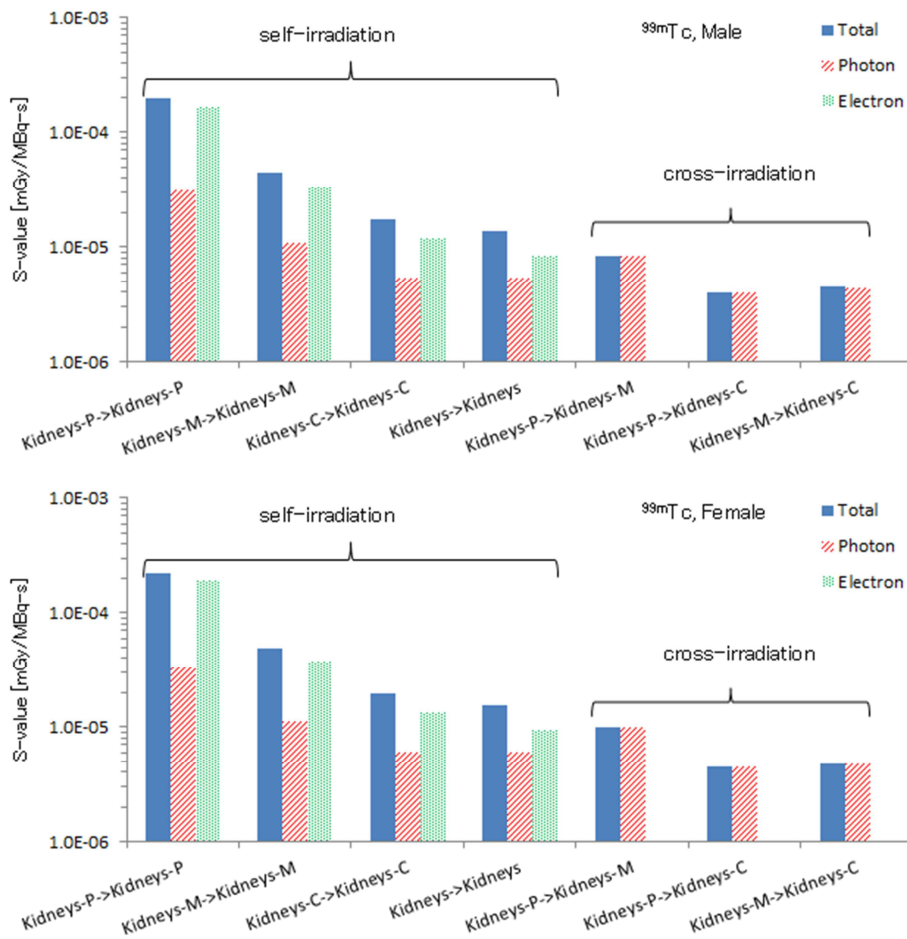


Figure 3. S-values of  $^{99m}\text{Tc}$  for kidneys in the ICRP adult male and female voxel phantoms.

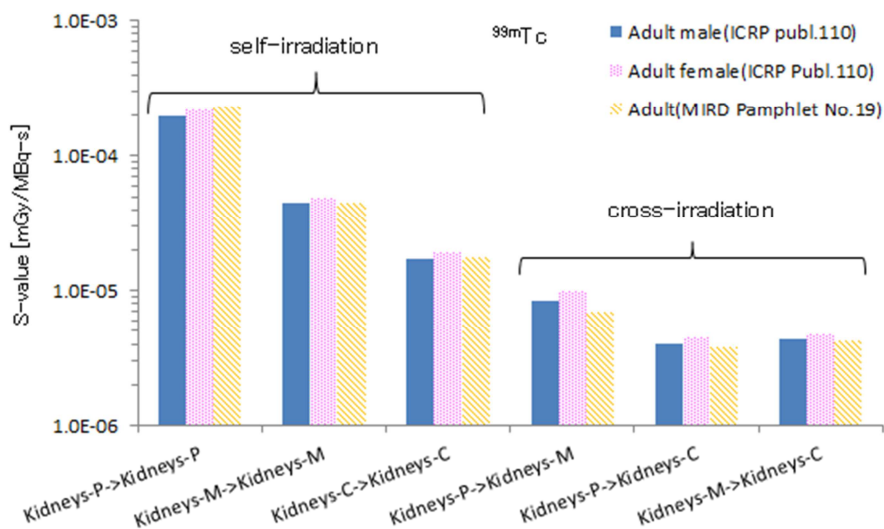


Figure 4. Comparison of S values of  $^{99m}\text{Tc}$  for multi-region models between adult male and female.

# Investigation of backscatter factor in mammography using EGS5

H. Numamoto<sup>1</sup>, T. Ishii<sup>1</sup>, Y. Hirai<sup>2</sup>, S. Koyama<sup>1</sup>

<sup>1</sup>*Department of Radiological Technology, Graduate School of Medicine, Nagoya University*

<sup>2</sup>*School of Health Sciences, Faculty of Medicine, Nagoya University*

*1-1-20 Daiko-Minami, Higashi-ku, Nagoya 461-8673, Japan*

*e-mail: numamoto.hitomi@c.mbox.nagoya-u.ac.jp*

## Abstract

In this study, backscatter factors (BSF) in mammography for W / Rh were estimated using Electron Gamma Shower ver. 5 Monte Carlo simulation code. Based on the exposure model proposed by Kramer et al., PMMA phantom and compression plate were simulated. Our results show that BSF for W / Rh are 1.11-1.13 for tube voltage ranges in 24-32 kV. From this result, it became possible to calculate an entrance surface dose in mammography.

## 1. Introduction

Owing to the rise in the incidence of breast cancer, mammographic examination has become a frequently used diagnostic tool. However, since the glandular tissues within the female breast are the most sensitive to radiation, mammographic examinations pose some risk of radiation-induced carcinogenesis. Hence, it is important to evaluate the radiation exposure dose in the glandular tissues. Generally, dose estimation in mammography is done in terms of the average glandular dose (AGD) [Gy]. The equation for AGD is given as

$$AGD = K \times g \times c \times s \quad (1)$$

where  $K$  is the incident air kerma at the upper surface of the breast phantom measured without backscatter [Gy],  $g$  is the incident air kerma to AGD conversion factor,  $c$  is a correction factor that accounts for any deviation from the assumed breast composition of 50% glandularity, and  $s$  is a factor that corrects for any difference from the original tabulation by Dance (1990), arising from the use of a different X-ray spectrum [1, 2]. However, since low-energy X-rays are used in mammographic examinations, entrance surface dose with backscatter (ESD) [Gy] would be higher than in general radiography, such as during chest X-ray examination. Therefore, in mammography, evaluation of ESD is also important in addition to AGD. ESD is given by

$$ESD = K \times BSF \quad (2)$$

where  $K$  is the incident air kerma at the upper surface of the breast [Gy] and BSF is the backscatter factor. Standard mammography BSF data are available, as recommended by European Protocol on Dosimetry in Mammography (European Commission 1996) [3]. BSF data for mammography have also been calculated using Monte Carlo methods by Kramer et al. [4]. These data are available for the following target/filter combinations: molybdenum/30  $\mu$ m molybdenum (Mo/Mo), molybdenum/25  $\mu$ m rhodium (Mo/Rh), rhodium/25  $\mu$ m rhodium (Rh/Rh), but not for tungsten/50  $\mu$ m rhodium (W/Rh).

In this study, backscatter factor in mammography has been investigated for W/Rh target/filter combination using EGS ver. 5 (EGS5), and a relationship established between ESD and AGD.

## 2. Materials and Methods

### 2.1 Confirming the consistency of the simulation method

#### 2-1-1 Monte Carlo simulation method

In order to validate the reliability of our simulation studies, we used a breast geometry similar to that used by Kramer et al. [4]. Figure 1 shows the geometry used in the simulation. The geometry was created with HOWFAR in the EGS user code. In order to represent the average compressed breast, a semicircular phantom with 10 cm radius and 5 cm thickness was used in the simulation studies. The X-ray focus to skin distance was 65 cm and the X-ray field was  $20 \times 24 \text{ cm}^2$ . The point of scoring deposit energy on the phantom was at a distance of 6 cm from the chest wall side. The phantom material was polymethylmethacrylate (PMMA). A 3 mm PMMA compression plate was also simulated and placed between the radiation source and the phantom. For the calculations, mammographic X-ray spectra were obtained from [5] for the following target/filter combinations: molybdenum/30  $\mu\text{m}$  molybdenum (Mo/Mo) and molybdenum/25  $\mu\text{m}$  rhodium (Mo/Rh). The tube voltage ranges of these spectra were in 28–32 kV. The number of photons was  $4.0 \times 10^8$  and the fractional standard deviation in the rectangular area was less than 0.2% in order to reduce the statistical error.

#### 2-1-2 Calculation and comparison of BSF

BSF was calculated using the Monte Carlo simulation method of Kramer et al. [4]. To assess the validity of our simulation, we calculated  $BSF_{MC}$  from the following relation and compared them with the values given in literature [4]:

$$BSF_{MC} = K_a^{ph} / K_a \quad (3)$$

where  $K_a^{ph}$  is the air kerma at a point on the surface of the phantom, and  $K_a$  the air kerma at the same point without the phantom. The scoring volume was defined as a cuboid ( $1 \text{ cm} \times 1 \text{ cm} \times 0.2 \text{ cm}$ ) centered at the point of reference, with an area of  $1 \text{ cm} \times 1 \text{ cm}$  facing the incident radiation and with one half of its thickness (= 0.1 cm) embedded into the phantom and the other half (= 0.1 cm) located outside the phantom [4]. The interior of the scoring volume was assumed to be air.

In order to evaluate the error range of BSF, we calculated the percent difference (PD) between  $BSF_{MC}$  and BSF. PD is given by

$$PD = \frac{BSF_{MC} - BSF}{BSF} \times 100 [\%] \quad (4)$$

where  $BSF_{MC}$  represents the backscatter factor calculated by us using Monte Carlo simulation, and BSF that calculated by Kramer et al. [4].

### 2.2 Backscatter factor for W/Rh

The above described simulation geometry (Figure 1) and the mammographic X-ray spectrum of W/Rh were used in the Monte Carlo simulation and calculation of  $BSF_{MC}$  for W/Rh.

From equations (1) and (2), a relationship between AGD and ESD was determined by substituting the values for  $g$ ,  $c$ ,  $s$  and  $BSF_{MC}$ . These values used in the calculations follow those given by Dance [2].

### 3. Results

We compared our backscatter factor calculated values ( $BSF_{MC}$ ) with those from the literature (BSF). Tables 1-3 show the values of  $K_a^{ph}$ ,  $K_a$  and the PD between  $BSF_{MC}$  and BSF. Table 1 shows that for Mo/Mo, PD was less than  $\pm 1.17\%$ . Likewise, for Mo/Rh, PD was less than  $\pm 0.91\%$  (Table 2), and for Rh/Rh, PD was less than  $\pm 1.02\%$  (Table 3).

Table 4 shows the values of  $K_a^{ph}$ ,  $K_a$  and  $BSF_{MC}$  for W/Rh. It can be seen that  $BSF_{MC}$  for W/Rh lies in the range 1.11–1.13 for tube voltages of 24–32 kV.

Table 5 shows the relationship between AGD and ESD for W/Rh. It is evident that for each tube voltage, ESD is about 4.5–5.5 times higher than AGD.

### 4. Discussion

The very small (less than  $\pm 1.17\%$ ) percent differences (PD) observed between our backscatter factor values ( $BSF_{MC}$ ) and the corresponding values from the literature [4] (BSF) for all the three target/filter combinations (Tables 1–3) validate the reliability of our simulation method used in the calculation of  $BSF_{MC}$  for W/Rh.

Our  $BSF_{MC}$  values for W/Rh (Table 4) for tube voltages in the range 24–32 kV are 1.11–1.13. The spectrum of W/Rh is composed of a continuum of X-rays, and is significantly different from the X-ray spectrum of Mo/Mo, Mo/Rh, Rh/Rh, etc. However, our  $BSF_{MC}$  values for W/Rh are not very different from the conventional BSF values. In addition, the tendency of BSF to increase with increasing tube voltage remains the same. This indicates that the shape of the X-ray spectrum does not affect BSF. Our W/Rh  $BSF_{MC}$  values could thus be used in the calculation of ESD in mammography.

Our results on AGD versus ESD (Table 5) establish that the entrance surface dose is always much larger than the average glandular dose. It is recommended in general guidelines that AGD in one mammographic examination should not exceed 2 mGy, and actual AGD is about 1.2mGy. This implies that in one mammographic examination ESD will be about 5-10 mGy. This elucidates the importance of knowing the actual entrance surface dose values, not just the average glandular dose values.

### 5. Conclusions

The backscatter factor of W/Rh was estimated using EGS5. It became possible to calculate ESD for W/Rh in the same way as in conventional mammography. Generally, dose estimation in mammography is done using AGD. We have shown that it is necessary to take into account the entrance surface dose in addition to the average glandular dose because ESD is much higher than AGD.

## References

- 1) Dance, D. R. “Monte Carlo calculation of conversion factors for the estimation of mean glandular breast dose”, *Phys. Med. Biol.* 35, 1211-1219 (1990)
- 2) Dance, D. R., Skinner, C. L., Young, K. C., Beckett, J. R., Kotre, C. J. “Additional factors for the estimation of mean glandular breast dose using the UK mammography dosimetry protocol”, *Phys. Med. Biol.* 45, 3225-3240 (2000)
- 3) European Commission 1996 European Protocol on Dosimetry in Mammography EUR 16263 (Luxembourg: European Commission)
- 4) R Kramer, G Drexler, N Petoussi-Hens, M Zankl, D Regulla and W Panzer “Backscatter factors for Mammography calculated with Monte Carlo methods”, *Phys. Med. Biol.* 46, 771-781 (2001)
- 5) Horst Aichinger, Joachim Dierker, Sigrid Joite-Barfuß, Manfred Säbel, (2004) “*Radiation Exposure and Image Quality in X-Ray Diagnostic Radiology*” Ohmsha

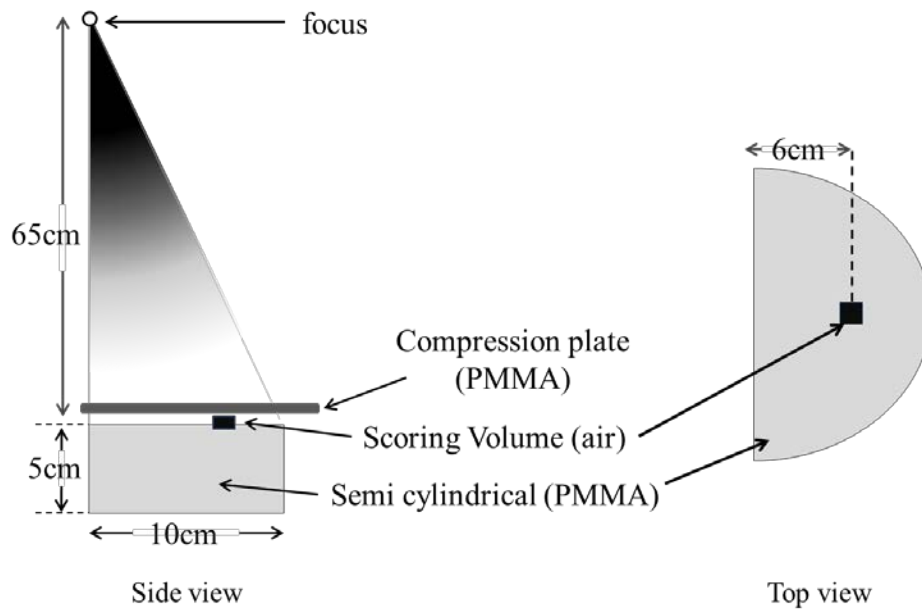


**Figure 1.** Monte Carlo simulation Geometry for calculation of backscatter factors

**Table 1.** A percent difference from the BSF of literature value for Mo/Mo

Tube voltage [kV]	$K_a^{ph} [mGy]$	$K_a [mGy]$	BSF <sub>MC</sub>	BSF	PD [%]
24	$1.46 \times 10^{-5}$	$1.36 \times 10^{-5}$	1.07	1.08	-0.65
26	$1.46 \times 10^{-5}$	$1.35 \times 10^{-5}$	1.08	1.09	-0.62
28	$1.45 \times 10^{-5}$	$1.34 \times 10^{-5}$	1.09	1.10	-1.07
30	$1.44 \times 10^{-5}$	$1.31 \times 10^{-5}$	1.10	1.11	-1.09
32	$1.44 \times 10^{-5}$	$1.31 \times 10^{-5}$	1.10	1.11	-1.17

**Table 2.** A percent difference from the BSF of literature value for Mo/Rh

Tube voltage [kV]	$K_a^{ph} [mGy]$	$K_a [mGy]$	BSF <sub>MC</sub>	BSF	PD [%]
24	$1.45 \times 10^{-5}$	$1.34 \times 10^{-5}$	1.09	1.09	-0.40
26	$1.44 \times 10^{-5}$	$1.31 \times 10^{-5}$	1.10	1.10	0.03
28	$1.44 \times 10^{-5}$	$1.30 \times 10^{-5}$	1.10	1.11	-0.46
30	$1.43 \times 10^{-5}$	$1.29 \times 10^{-5}$	1.11	1.12	-0.91
32	$1.41 \times 10^{-5}$	$1.28 \times 10^{-5}$	1.10	1.11	-0.59

**Table 3.** A percent difference from the BSF of literature value for Rh/Rh

Tube voltage [kV]	$K_a^{ph} [mGy]$	$K_a [mGy]$	BSF <sub>MC</sub>	BSF	PD [%]
24	$1.44 \times 10^{-5}$	$1.32 \times 10^{-5}$	1.09	1.09	-0.09
26	$1.41 \times 10^{-5}$	$1.28 \times 10^{-5}$	1.10	1.10	-0.04
28	$1.39 \times 10^{-5}$	$1.25 \times 10^{-5}$	1.11	1.12	-0.89
30	$1.37 \times 10^{-5}$	$1.23 \times 10^{-5}$	1.12	1.13	-1.02
32	$1.35 \times 10^{-5}$	$1.20 \times 10^{-5}$	1.12	1.13	-0.75

**Table 4.** BSF<sub>MC</sub> for W/Rh

Tube voltage [kV]	$K_a^{ph} [mGy]$	$K_a [mGy]$	BSF <sub>MC</sub>
24	$1.43 \times 10^{-5}$	$1.29 \times 10^{-5}$	1.11
26	$1.40 \times 10^{-5}$	$1.25 \times 10^{-5}$	1.12
28	$1.38 \times 10^{-5}$	$1.23 \times 10^{-5}$	1.12
30	$1.36 \times 10^{-5}$	$1.21 \times 10^{-5}$	1.12
32	$1.35 \times 10^{-5}$	$1.19 \times 10^{-5}$	1.13

**Table 5.** A relationship between AGD and ESD for W/Rh

Tube voltage [kV]	BSF <sub>MC</sub>	$g$	$c$	$s$	ESD/AGD
24	1.11	0.194	1.150		5.487
26	1.12	0.209	1.145		5.149
28	1.12	0.218	1.143	1.042	4.936
30	1.13	0.226	1.141		4.795
32	1.13	0.233	1.139		4.656